Memoirs of the Faculty of Science, Kyoto University, Series of Physics, Astrophysics, Geophysics and Chemistry, Vol. XXXVII, No. 3, Article 2, 1989

MEASUREMENT OF THE DEPOLARIZATION PARAMETER $K_{y'}$ IN p-^{2}H ELASTIC SCATTERING AT E_p=65 MeV

By

Masanobu NAKAMURA

Department of Physics, Faculty of Science, Kyoto University, Kyoto 606, Japan

(*Received January 30, 1988*)

Abstract

A newly designed spectrograph has been constructed in order to measure spin transfer coefficients. The depolarization parameter $K_{y'}$ in the elastic scattering of 65 MeV polarized protons from deuterium has been measured using the spectrograph and a multi-foil polarimeter. Faddeev calculations using various nucleon-nucleon (N–N) interactions in a separable representation are compared with the data. The measured $K_{y'}$ values are well reproduced by a calculation using the N–N interaction with a tensor force which is adjusted to reproduce the empirical mixing parameter of the $^3S_1$–$^3D_1$ partial waves. A separable representation of the Paris potential by means of EST method (PEST) does not reproduce the data well.

1. Introduction

Recent progress in experimental techniques as well as the theoretical treatment of the three-nucleon system allows us to investigate aspects of the nuclear force different from those exhibited in nucleon-nucleon (N–N) scattering. It is one of the most interesting problem in nuclear physics to investigate how to explain the three-nucleon system from our knowledge of two-nucleon interactions from nucleon-nucleon scattering. The binding energies of ^{3}H and ^{3}He and their electromagnetic form factors obtained from the electron scattering are compared with theoretical calculations. An extension to the three-body scattering state *i.e.* N–d elastic scattering or breakup reaction, is very interesting. Recent progress in experimental techniques allows us to measure not only differential cross section and analyzing power but spin transfer coefficients and spin correlation functions. Can we explain all of the observed data from our knowledge of two-nucleon interactions? Can we derive any information about the nucleon-nucleon interaction which cannot be derived from the two-nucleon system alone?

The N–N force is usually obtained by fitting the two-body scattering data and the properties of the deuteron. Most of the on-energy-shell properties of the two-nucleon potential are determined from phase shift analyses of the N–N scattering. In 1980's an energy-dependent and single-energy analysis of N–N scattering below 1 GeV laboratory kinetic energy was done (ref. 1). However, the mixing parameter

ε_1 of the $^3S_1$ and $^3D_1$ partial waves remains still relatively uncertain because of the strong correlation between ε_1 and the $^1P_1$ phase shift and certain experimental difficulties (ref. 2). On the other hand phenomenological potentials were proposed *e.g.* the Paris potential which derived from the dispersion theory of pion-nucleon scattering (ref. 3) or the Bonn potential which derived from one boson exchange model (ref. 4). It is to be noted that even these modern potentials differ substantially in the prediction for certain observables for instance the spin correlation parameter $C_{y,y}$ in n–p scattering. An additional knowledge of the on-shell N–N interaction is expected to be obtained from some observables of the p–^{2}H system. Moreover, the N–N data alone are not sufficient to determine the off-shell behavior of the interaction. New insights into the off-shell behavior can be expected from the study of the p–^{2}H system.

The three-nucleon scattering system can be treated theoretically using the Faddeev equation (ref. 5). For computational convenience, separable potentials have served as essential tools for practical applications to few-nucleon scattering systems. In 1965 Aaron, Amado and Yam calculated with Yamaguchi type separable potentials in the S waves (ref. 6), and the comparison of their calculation with experimental cross section of p–d scattering was interested. Since the multiple scattering series for elastic scattering of neutron-deuteron for L=0 series converges only slowly, the numerical treatment was improved and checked. Two different approaches have been used to solve the three-nucleon scattering problem. One of them is to use separable t-matrices derived from phenomenological separable potential or a separable representation of any potentials by means of EST method (ref. 7). The other is to use a two-body off-shell t-matrix obtained from realistic local potentials. Recently, separable N–N potentials have been greatly improved, to an extent that detailed comparisons between the calculated and experimental results for the N–^{2}H system become significant. For example, Faddeev calculations of p–^{2}H polarization transfer coefficients at E_p=65 MeV by Koike and Taniguchi (ref. 8) showed that differences in the $^3S_1$–$^3D_1$ interaction appear distinctly in these observables. Measurements of the depolarization parameter are expected to provide a check on the relative importance of the on-shell and off-shell effects.

Table 1. 20 observable subsets.
proton a: unpol v: vector pol.
deuteron A: unpol V: vector T: tensor

pd pd	NAME
$aA\ aA$	sigma
$aA\ aV{=}aV\ aA$	A_y (d, d)
$aA\ vA{=}vA\ aA$	A_y (p, p)
$aA\ vV{=}vV\ aA$	C_{yy}
$aV\ aV$	$K_y{}^{y'}$ (d, d)
$vA\ aV{=}aV\ vA$	$K_y{}^{y'}$ (p, d) or (d, p)
$vA\ vA{=}vA\ vA$	$K_y{}^{y'}$ (p, p)
$vV\ vA{=}vA\ vV$	
$vV\ aV{=}aV\ vV$	
$aT\ aA$	A_{yy}
$aT\ aT$	$K_{yy}{}^{yy'}$
$aT\ aV{=}aV\ aT$	$K_{yy}{}^{y'}$ (d, d)
$aT\ vA{=}vA\ aT$	$K_{yy}{}^{y'}$ (d, p)
$aA\ vT{=}vT\ aA$	$C_{yy,y}$
$aT\ vT{=}vT\ aT$	
$aT\ vV{=}vV\ aT$	
$aV\ vT{=}vT\ aV$	
$vT\ vA{=}vA\ vT$	
$vT\ vT$	
$vT\ vV{=}vV\ vT$	

Sets of polarization experiments can yield complete or partial useful information

about the dynamics of the p–^{2}H elastic scattering. The reaction under study has, in the presence of only the Lorentz invariance, $X=2\times3\times2\times3=36$ amplitudes. When the time reversal invariance and parity conservation are imposed, the number of independent amplitudes reduces to 12. The number of bilinear combination of amplitudes is therefore 144, which then is also the number of linearly independent observables. Of course, a set containing at least 23 of them is needed to determine the 12 amplitudes unambiguously. We know that by no means all sets containing 23 observables will determine the amplitudes. A relatively simple subset of experiments can be listed in the transversity formalism which by itself determines all the magnitudes of complex amplitudes (ref. 9). This subset (see table 1), which obviously contains 12 experiments for the reaction under considering, determines the magnitudes without the ambiguity (discrete or continues).

2. Polarization Measurement Technique

2.1 General

In order to get the information of the polarization quantity we use three facilities:

1. polarized beam,
2. polarized target,
3. polarimeter for emitted particles.

The polarized beam is obtained by accelerating the beam produced from a polarized ion source or selecting the secondary beam which is polarized after first scattering. The polarized proton ion source has been improved on the beam intensities 30 times per 5 years since 1965 and the accelerating beam intensity is as high as the ordinary unpolarized beam intensity for low energy accelerators (tandem Van de Graaff accelerators and cyclotrons). The polarized beam is also accelerating by high energy accelerators (linear accelerators and synchrotrons). Now a first order spin observable *e.g.* analyzing power can be measured with so high precision as for differential cross sections. Progress in cryogenic technique allows us to polarize hydrogen atoms and many other atoms. So the combination of 1 and 2 allows us to measure the second order spin observables *e.g.* spin correlation functions. On the other hand measurements of the polarization of emitted particles is far from its ideal measurement which can detect the individual polarization. We can obtained the information proportional to the polarization of outgoing particles but the detecting efficiency is very low.

2.2 Polarimeter for emitted particles

To measure the polarization of emitted particles, we want to measure other physical quantities (*e.g.* energy, scattering angle etc.). It is important for an efficient measurement that a detecting facility satisfies the following conditions:

A. polarization quantity,
   1) high effective analyzing power known with a good accuracy,
B. other than polarization quantity,
   2) good energy resolution for the first scattering,

3) to accept a broad energy range,
4) good scattering angle resolution,
5) good time resolution,
6) to allow a particle identification,

C. general,

7) high detecting efficiency,
8) to allow a high rate of good events,
9) low background,
10) simplicity of the set-up.

There are three methods for measurements of the polarization of emitted particles:

a) Stern-Gerlach,
b) particle correlation,
c) double scattering.

(a) If a particle with a magnetic moment experience a magnetic field with a gradient rather than a uniform field, the spin states are subjected to opposing forces. This method is useful for the particle with a large magnetic moment *e.g.* electron. This is also suitable for measurement of the polarization of cold neutron beam ($\lambda > 0.5$ nm). But it is difficult to use for heavier particles and higher energy particles.

(b) If a particle is unstable and a correlation between decaying particles is measured, the polarization of the particle before the decay can be obtained. But this is not suitable for stable particles like protons.

(c) We have to rely on double scattering.

2.3 Double scattering method

To determine the polarization of the scattered particles, at present we inevitably have to use a polarimeter which is based on the measurement of left-right asymmetry in scattering from analyzer target (see fig. 1). An efficient polarimeter as well as an intense polarized beam plays an important role in the polarization transfer experiment. If particles are charged and loss the energy in the second target, the thickness of the target is limited and the efficiency become low. The scattering probability of protons from hydrogen is shown in fig. 2. The number of particles incident on the polarimeter is less in several orders of magnitude than that of incident particles on the first target.

Many efforts have been devoted to the construction of polarimeters at several laboratories (refs. 10–17). In polarimeters for several hundreds MeV protons (refs. 10–12), multi-wire proportional chambers (MWPC) (or drift chambers (MWDC)) are used to reconstruct proton trajectories and to cover a large solid angle. But elastic and inelastic scattering from the analyzer trarget are not distinguished. For protons below 100 MeV, the various polarimeters (13–17) with thick analyzer targets have been developed keeping a good separation between elastic scattering and inelastic scattering: the polarimeter with a Si–SSD as an analyzer target (ref. 13), the polarimeter using a series of carbon targets with an elaborated shaped degrader (ref. 14), the polarimeter used in conjunction with an Enge split-pole spectrograph

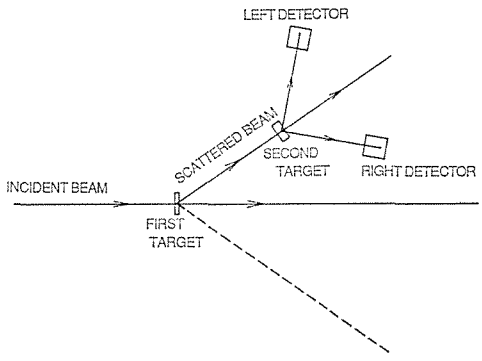

Fig. 1. Schematic diagram of a double scattering experiment.

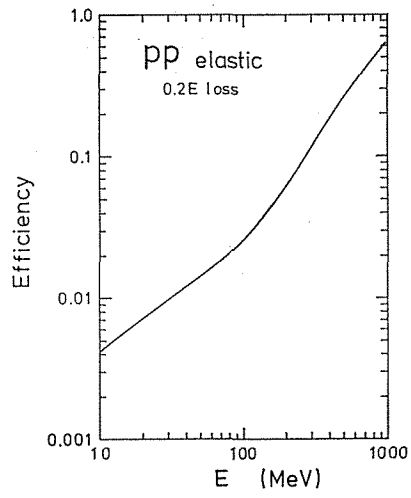

Fig. 2. Energy dependence of the scattering probability of protons from Hydrogen in which the proton energy loss is 20% of the incident energy.

and so on. The principal advantage to use a magnetic analyzer is a decoupling of energy resolution from counting rate considerations. However, they partially satisfy the above requirements. So there is a room for improvements in the effective analyzing power and the overall efficiency.

3. Polarization Spectrograph DUMAS (refs. 18–19)

3.1 Principle of the polarization spectrograph DUMAS

A new type of spectrograph named DUMAS (Dual MAgnetic Spectrograph) was constructed at the Research Center for Nuclear Physics (RCNP), Osaka University (fig. 3). Suppose a dual magnetic spectrograph system in which two spectrographs join in cascade so as to cancel out their momentum dispersion with each other. A thin position sensitive particle counter which is traversed by the particles, will be set at the first focal plane *i.e.* the focal plane of the first part of DUMAS. While at the second focal point *i.e.* the focal point of the second part of DUMAS, the second target system will be set for double scattering measurements. One can combine signals from the first focal plane counter tagging particle momenta with those from left- and right-counter systems associated with the second target and achieve high efficient asymmetry and/or spin transfer measurements for the reaction particles over the wide range of their momenta simultaneously.

Since DUMAS has two foci, we realize the following characteristics:

1) At the first focal line;
   a) Large dispersion and high resolution.
   b) Broad energy range:

This may be useful to measure the continuum spectrum and the scattering from the thick target.

2) At the second focus point;

c) Small image:

It allows the side counter to detect only the second scattering particles and not to count the unscattered ones.

d) Parallel beam:

This realize a long target region (many targets). This fact is important

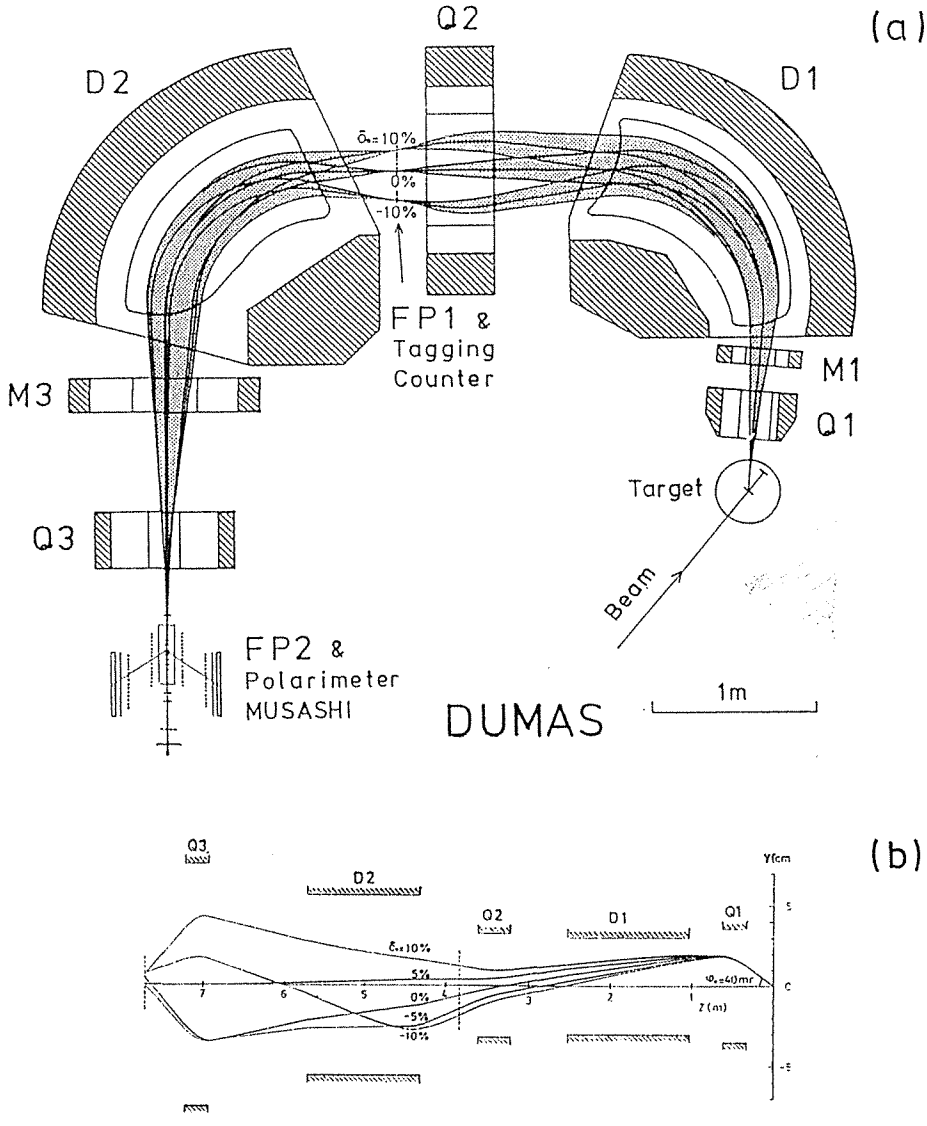

a) plane view, b) side view

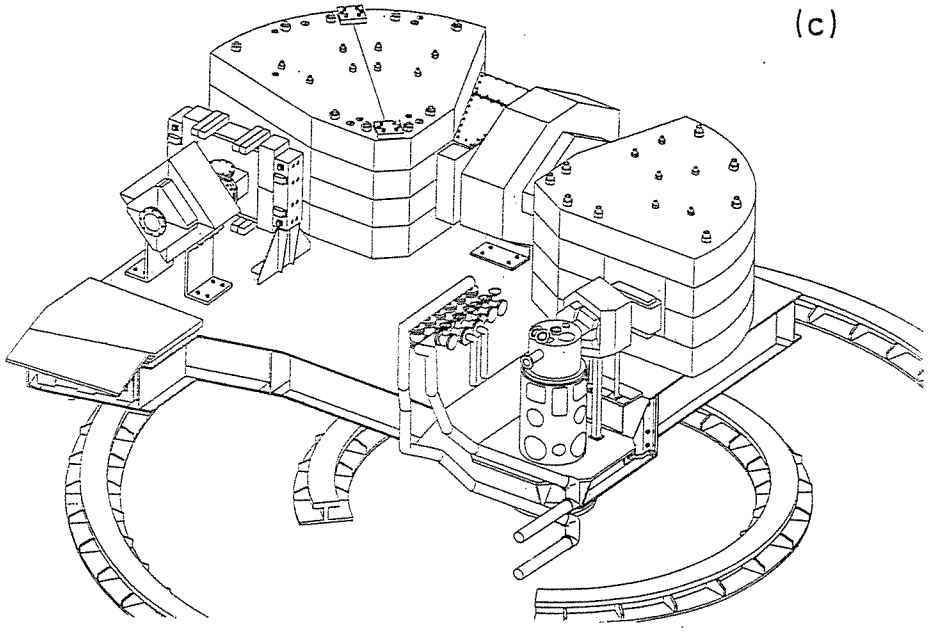

c) bird-eye view

Fig. 3. Schematic layout of the polarization spectrograph DUMAS.

to reduce the geometrical asymmetry on the second target.

3) From object (TP) to image (FP2);

e) Overall deflection angle:

The overall deflection angle from TP to FP2 is almost constant independently of orbit radius or injection angle to the system in the first order. This fact is important especially in measurements of horizontal components of polarization such as a $K_x^{x'}$ measurement, because deviations of deflection angles cause different spin-precession angles in the magnetic field.

f) Small vertical angle deflection:

This fact is important especially in measurements of vertical components of polarization such as a $K_y^{y'}$ measurement, because the vertical angle deflection causes a depolarization by the spin-recession angles in the magnetic field.

g) Equal flight length:

The path lengths from TP to FP2 are the same in the first order for particles with the same momentum. This may be useful to reduce chance coincident events in the case of correlation measurements or to identify particles by a TOF technique when DUMAS is used as a momentum filter.

3.2 Design of DUMAS

In order to resolve peaks in the momentum spectrum of the elastic and inelastic scattering from the medium unclei ($A<100$) and to measure broad peaks or continuum states, we set the design goal of this energy resolution ($\Delta E/E$) to be 1/1000, energy broadness $\pm 20\%$ and solid angle 10 msr.

For a broad momentum range spectrograph with a moderate momentum resolution, a structure of quadrupole-dipole-quadrupole (QDQ) is usually recommended (ref. 20). Thus the first part of DUMAS has been adopted this structure of QDQ. The second part of DUMAS plays roles of the dispersion cancellation and the particles beam refocusing and thus has the same structure with that of the first except its reverse order of element arrangement. Therefore the spectrograph DUMAS was preferred to have a structure of QDQDQ as a total. The main roles of each magnet group are summarized bellow.

Front quadrupole Q1: gain of the resolving power and an auxiliary function to increase the acceptance angle in the vertical direction.

First dipole D1: deflection and dispersion. Corrections for the higher-order focusing and tilt angle of the first focal plane can be achieved through proper shaping of the field boundaries.

Middle quadrupole Q2: adjustment of location of the horizontal focusing point and tilt angle of the first focal plane and hence the magnification as well as the dispersion of the first focal part of DUMAS.

Second dipole D2: generation of the dispersion for cancellation with that of the first part of DUMAS. Corrections for the higher-order focusing in the same way as in the case of D1.

Post quadrupole Q3: adjustment of location of the second focal point as well as the size of the dispersion of the second part of DUMAS.

In the first phase, a computer code ORBIT (ref. 21) was used. This program was developed by Morinobu and a composite of a parameter optimization program and the program TRIO (ref. 22) written within the third order approximation. The edge angles of the D1 and D2 magnet pole boundaries with respect to the normal of the central trajectory were determined to make the dispersion cancellation easy besides achieving two directional focusing at both the first focal plane and the second focal point. Special cares were paid to achieve the higher order correction which was performed in three phases over the wide range of particle momenta. Relevant second-order parameters, namely, curvatures of the D1 and D2 magnet pole boundaries were determined such that the second-order transfer coefficient $(x|\ \theta\ \delta)$ vanishes at the first focal plane. This condition, $(x|\ \theta\ \delta)=0$, is indispensable to make the dispersion zero at the second focal point over the wide range of particle momenta and necessarily to make the first focal plane normal with respect to the central trajectory.

For the purpose refining the higher order calculations, the program named OPTRACE (ref. 23) was improved by Takayama. This program was an automatic

parameter search code which was composed of a parameter optimization program based on the Newton's method and the program RAYTRACE (ref. 24). The program OPTRACE was found to have a remarkable effect in increasing optimization speed. In the second phase, the same calculation procedure has been repeated by using the program OPTRACE in order to reduce aberrations at the second focusing point as well as those at the first focal line. In this procedure, it was concluded that several sextupole fields have to be introduced in combination besides those generated by curving the D1 and D2 magnet pole boundaries. Furthermore, the combination required is rather complex and their strength is considerably large being beyond the scope of magnet pole boundary curving usually achieved. Hence, three additional sextupole fields were introduced by shaping magnet pole faces inside the dipoles D1 and D2. Additional improvement on the aberration reduction and hence on gaining the solid angle of particle acceptance was made by superposing the sextupole field on the quadrupole field of Q1. The magnet pole faces of Q1 were so shaped as to generate the combined quadrupole and sextupole fields. In the similar way the magnet pole faces of Q2 were shaped to superpose weak sextupole and octupole field on the quadrupole field.

Table 2. Specifications of the main magnets in the polarization spectrograph DUMAS.

Dipole Magnets

		D1	D2	
Gap		60	118	mm
Deflection angle		95	90	deg.
Maximum current	(main coil)	37000	74000	AT/coil
	(correction coil)	2500	5000	AT/coil
Maximum field	(dipole)	15	15	kG
	(sextupole)	−6.3 0	7.4 −2.1	G/cm^2
	(octupole)	0 0	−130 −20.8	mG/cm^2
	(decapole)	0 0	0 2.8	mG/cm^2
Total weight		18	21	ton

Quadrupole Magnets

		Q1		Q2	Q3	
		left*	right*			
Maximum current	(main coil)	18600	10300	36000	18300	AT/coil
	(correction coil-1)	1900	1060	760	5200	AT/coil
	(correction coil-2)	0	0	1500	4100	AT/coil
Maximum field	(quadrupole)	−1.15		0.49	−0.75	kG/cm
	(sextupole)	81		0.22	0	G/cm^2
	(octupole)	0		−5.5	0	mG/cm^2
Total weight		0.5		3.8	1.1	ton

*with respect to the particle beam direction

3.3 Design and construction of magnets

The principal specifications of these magnets are tabulated in table 2. For all magnets, rather narrow tolerances have been set in machining and positioning the pole pieces, since errors in the optical geometry may seriously deteriorate the performance of the spectrograph. In making magnets, especially pole pieces, NC (numerically controlled) machines were fully used. All coils were made of copper hollow conductors insulated with epoxy-impregnated glass tapes. All magnets are also equipped with correction coils for achieving the balance of field strength among the magnets.

The computer program TRIM (ref. 25) was extensively used in the magnet design work. In this design work, Poisson's equation was solved within the space with two dimensional cartesian coordinate. For calculating fields inside the D1 and D2

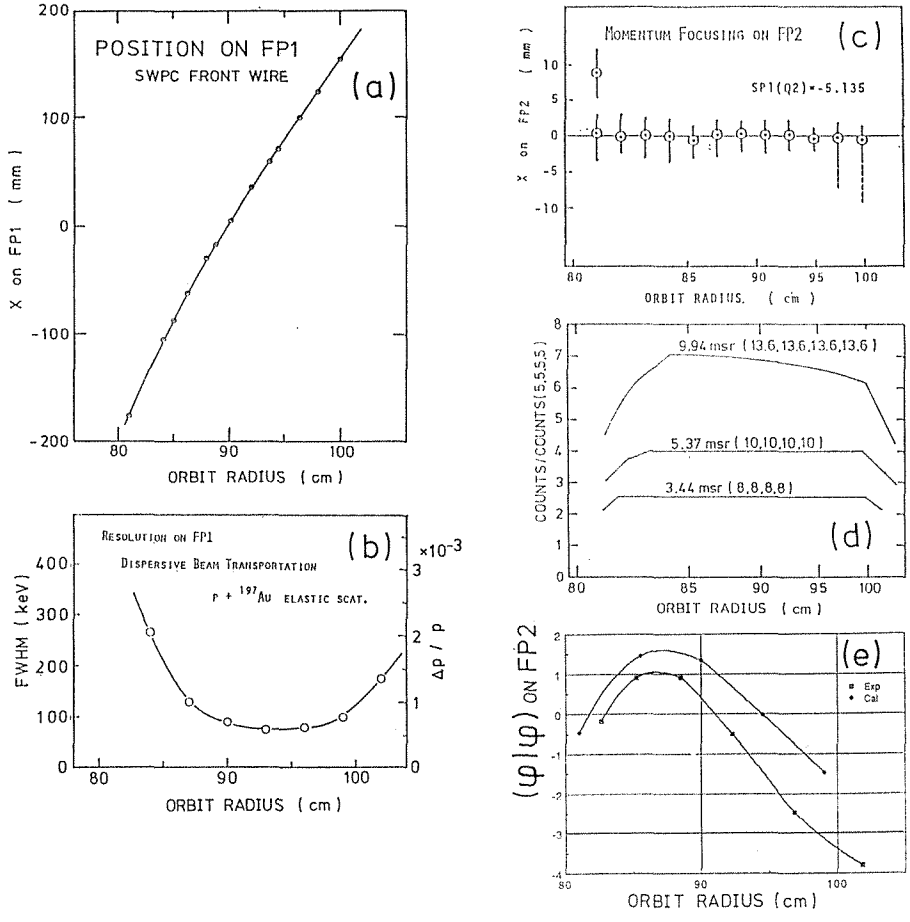

Fig. 4. Results of the ion optical measurements:
a) position on FP1, b) overall resolution on FP1, c) momentum focusing on FP2, d) particle acceptance, e) vertical angle transfer coefficient $(\phi|\phi)$ from TP to FP2. All quantities are plotted as a function of the orbit radius.

magnets, cross-sections of the side yokes in the two dimensional space were readjusted so as the magnetic flux distributed in both side yokes to be equal as in the actual case. The pole piece faces of dipole magnets are shaped in appropriate equipotential curves to generate one or two kind of sextupole fields and higher multipole fields superposing on the dipole field. The curves have been approximated by the succession of steps (minimum height of 0.1 mm) for the case of NC machining. The corners of the pole edges are shaped in a Rogowski's curve which has also been approximated by the succession of steps.

3.4 Option

All these magnets are mounted on a carriage which can rotate from −60° (left) to 140° (right) around the center of the scattering chamber. A beam dump is available from −35° to −60° and it allows a low background measurement. A compact chamber with a mylar window is decoupled the vacuum of beam transport and the spectrograph. A sliding seal chamber is also available for measurements of heavy ions or very forward angle particles. DUMAS has three sets of slits. First one is in front of the Q1 and define the solid angle. Second one is after the Q2, just before the first focal line, and define the particle momentum. Third one is in front of Q3 after D2 and define the scattering angle when target material is gas. Around the scattering chamber 25 cm thick shields of mixed paraffin and iron sands were placed to reduce the X-ray, γ-ray and neutron backgrounds in the experimental hall.

Table 3. Achieved or confirmed properties of DUMAS.

Maximum energy	$E_{max}=110\ Z^2/A$ MeV
Orbit radius	$\rho=84$–98 cm
Spectrum range	$\pm 7.7\%$ in momentum ($\pm 15\%$ in energy)
Maximum solid angle	$\Delta\Omega_{max}>5.6$ msr (75 mr horizontal $\times$ 75 mr vertical)
Deflection angle	185°
Length of central orbit ($\rho=90$ cm)	$l=7.80$ m
Maximum deviation of the path length for particles with central momentum	$\Delta l/l=0.12\%$
1st focal plane	
Size	40 cm horizontal $\times$ 8 cm vertical
Energy dispersion	$\Delta x \cdot E/\Delta E=700$ mm ($\rho=98$ cm) 1015 mm ($\rho=84$ cm)
Tilted angle	0° (normal to the central orbit)
Energy resolution	$\Delta E/E=1/850$* (monochromatic beam transport) 1/350 (achromatic beam transport)
2nd focal point	
Energy dispersion	0 (less than 10 mm).
Spot size (FWHM)	7 mm horizontal $\times$ 5 mm vertical

*Solid angle: 24 mr horizontal $\times$ 54 mr vertical $=1.3$ msr

3.5 Ion optical measurements

The momentum resolution of this system depends on the orbit radius of particles in the dipole magnets and the properties of primary beam itself. The overall resolution measured on FP1 is plotted in fig. 4b as a function of the orbit radius. The open circles show the resolution when a primary beam is transported onto the target monochromatically. In a usual double scattering measurement, we use the achromatic beam transportation in order to transport a beam from the cyclotron onto the target without serious intensity loss. In the case of monochromatic beam transportation, less than 10% of an extracted beam reaches the target. All the data in fig. 4 were obtained using a single wire proportional counter as a position counter at the first focal plane, the position resolution of which is about 0.3 mm. Confirmed properties of DUMAS are summarized in table 3.

4. Counter System

The counter system consists of a position counter for momentum tagging placed at FP1, a polarimeter system named MUSASHI at FP2 and electronic circuits to read out signals from those counters.

4.1 Tagging counter (counter at the first focal plane)

The scattered protons were momentum-analyzed and focused dispersively on the first focal plane (FP1) of DUMAS (fig. 3). Since the particle flux at FP1 was quite high, we used a multi-wire proportional chamber (MWPC) as a position counter at FP1. The specifications of this counter are listed in table 4. A typical counting rate of this counter was 100–300 kcps exclusive of background caused by γ- and X-rays. The efficiency of this counter was better than 99% at the counting rate of 5 kcps per wire and the counting loss was allowable when measured particles were distributed in the wide range of the counter. However, when the particles were concentrated on a few wires, a serious reduction of the efficiency occurred. In such cases, a movable slit (tagging slit) positioned in front of the tagging counter was used in order to stop undesirable particles.

Since the tagging counter is installed on the focal plane, the angular spread of

Table 4. Specification of MWPCs.

	LL, RL (large)	LM, RM (middle)	XS, YS (small)	TAGGING
Wire spacing	2 mm	2 mm	1 mm	2 mm
Anode cathode gap	6 mm	6 mm	3 mm	8 mm
Effective region	350×350 mm²	350×200 mm²	70×70 mm²	400×80 mm²
Supplied voltage	4.7 kV	4.7 kV	3.7 kV	5.6 kV
Anode	20 μm gold-plated tungsten wire			
Cathode	125 μm Cu/Be			
Gas mixture	argon: isobutane: freon: methylal=66: 33: 0.3:4			

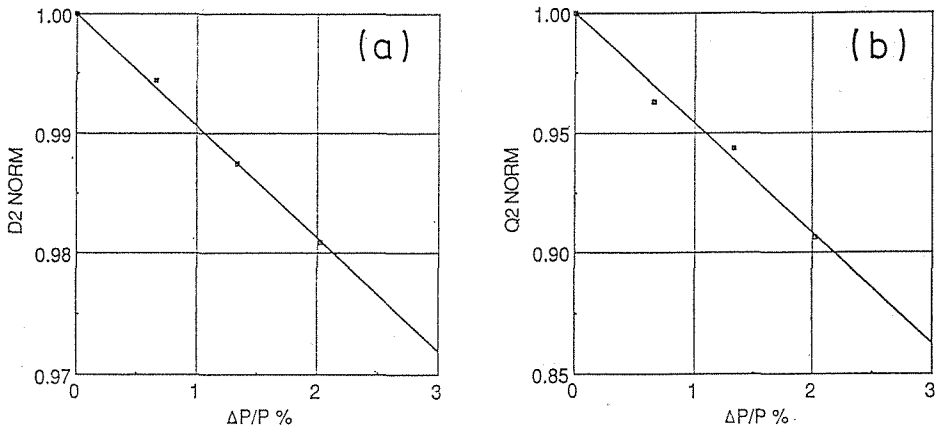

Fig. 5. *Correction of the strength for the energy loss in the tagging counter*: a) D2 magnet, b) Q2 magnet.

passing protons through the counter due to multiple Coulomb scattering does not cause a serious broadening of the image at the second focal point (FP2). The effect of the energy loss for protons in the counter is corrected by adjusting the strength of D2 and Q2 magnets (fig. 5).

4.2 **Multi-foil polarimeter MUSASHI** (ref. 26)

A scale drawing of the polarimeter MUSASHI is shown in fig. 6. The scattered or emitted protons from the first target may hit one of carbon foils, which are placed along the central axis of the polarimeter. The protons scattered from carbon foils are

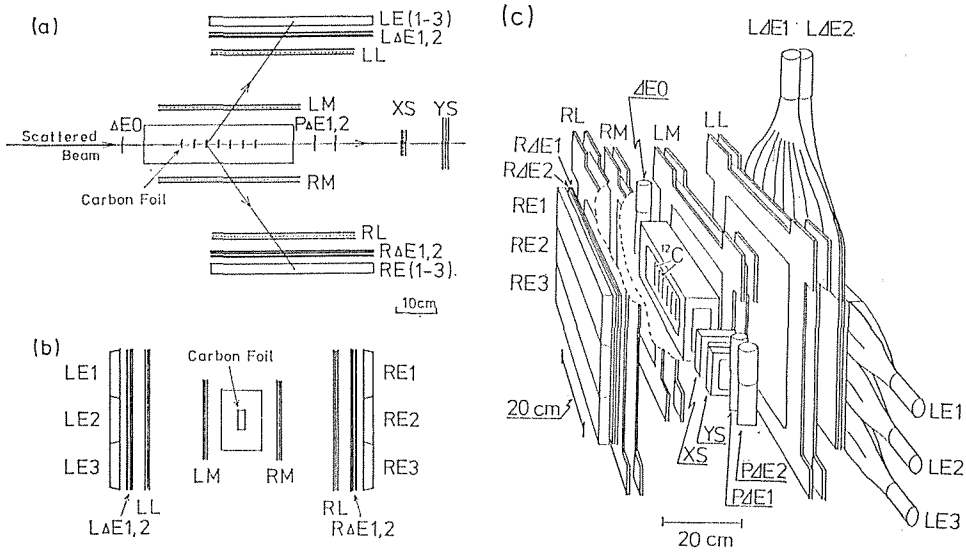

Fig. 6. Results of schematic layout of the multi-foil polarimeter MUSASHI: a) plane view, b) front view, c) schematic representation.

detected by a left or a right counter array; each consists of two MWPCs (LM and LL or RM and RL) and a set of plastic ΔE–E scintillators (LΔE1, LΔE2 and LE1–3 or RΔE1, RΔE2 and RE1–3). These MWPCs and plastic scintillators provided useful information for the energy and track reconstructions of scattered protons and the background reduction. Protons which were scattered from the carbon foil at scattering angles larger than 35° were accepted by a detector system. The whole polarimeter efficiency was $\sim 1 \times 10^{-3}$. It should be noted that in this polarimeter unscattered protons are not counted by the side counters.

A polarimeter at the second focal point (FP2) of DUMAS does not need to satisfy the requirement B (other than polarization quantity) and has to meet the requirement A (polarization quantity) and C (general). Each carbon target has a suitable thickness so that the elastic scattering from carbon is resolved by a plastic scintillator. To increase the scattering yield, we use a multi-foil of carbon. MWPCs and plastic scintillators are used as side detectors which allow the polarimeter to have a large solid angle acceptance from carbon targets. This polarimeter gives information on a scattering position, a scattering angle, and an energy for each scattered proton from carbon and so we can determine the Q-value for the second scattering with good resolution. The present method allows us to select the suitable angular region according to incident proton energies. It has a large effective efficiency and a large effective analyzing power in a wide energy region below 100 MeV.

The carbon foil is a flexible graphite NICAFILM with a measured density of ~ 1 g$\cdot$cm^{-3}. The size of carbon foil is 2 cm wide and 5 cm high. Each of carbon foil is spaced 3 cm apart to allow protons scattered at angles down to 20° to escape into side counter arrays without striking the next foil. The foil thickness is limited in order to avoid an overlap between elastic and inelastic scattering spectra. It can be chosen from among 40.0, 74.3, and 157 mg$\cdot$cm^{-2} thickness for practical use depending on the energy of the incident proton. Here we used the 157 mg$\cdot$cm^{-2} foil. The whole multi-foil of carbon is mounted in a chamber.

MWPCs are used as position counters which span a large solid angle of acceptance from carbon foils. The specifications of MWPCs are listed in table 4. Each MWPC consists of three wire planes: an anode wire plane is sandwiched between two cathode planes. A negative high voltage is applied to cathode wires, while anode wires are at ground. Signals from anode wires are fed to preamplifiers located near MWPCs through 1 m micro-strip-line flat cables (flat cable with low cross talk). Balanced signals from preamplifiers are transferred to CAMAC modules through 6 m twisted-pair lines. The filling gas is essentially the magic gas mixture (ref. 27) containing 0.3% of freon and mixed with argon bubbled through methylal to reduce deleterious effects of hydrocarbon accumulation on wires (ref. 28).

The plastic scintillation detector used to measure the proton energy (E-counter) is composed of three parts (LE1$\sim$3 and RE1$\sim$3, see fig. 6), which results in improved energy resolution and gives rough information on the azimuthal angle. The size of each scintillator is 40 cm wide, 12 cm high, and 25 mm thick. A single LE2 (RE2) counter provides an azimuthal angular acceptance of ± 10.5°, while a set of LE1$\sim$

LE3 (RE1~RE3) provides that of $\pm 28.9°$. The plastic scintillators L(R)ΔE1 (5 mm thick) and L(R)ΔE2 (3 mm thick) are placed between LL(RL) MWPC and the left (right) E-counter and they are 40 cm wide and 40 cm high. Light guides for these plastic scintillators are of a twisted type and are designed so as to transmit all the lights that enter within the acceptance angles at the input end. Each plastic scintillator of the E-counter is viewed by a HAMAMATSU R329 photo-multiplier tube (PMT) only at the each downstream end because of a narrow space between the polarimeter and the Q3 magnet of the spectrograph (see fig. 3). So, there is some position dependence for the lights accepted by the PMT. However the position information from MWPC telescopes allows us to correct the position dependence along plastic scintillators. The plastic scintillator ΔE0 of 5 cm wide, 7 cm high and 0.3 mm thick is located at the entrance of the polarimeter. A trigger signal is generated by the coincidence of ΔE0, L(R)ΔE1, L(R)ΔE2, and one of L(R)E-counters. Especially, ΔE0 plays an important role to reduce the background. The ratio of true events vs. triggered events is nearly equal to 100%. The plastic scintillators PΔE1 and PΔE2 are the same size as ΔE0 and mounted directly behind the carbon target chamber to count protons which have passed through carbon foils. The E-plastic scintillators and left and right ΔE scintillators are made of SCSN38, and ΔE0, PΔE1, and PΔE2 are NE102.

The carbon targets, profiles monitor counters (XS, YS), ΔE0, PΔE1 and PΔE2 are all mounted in the same movable rectangular frame. MWPCs (LL, LM, RL and RM) and ΔE–E telescopes are also attached to movable rectangular frames. Each corner of the rectangular frames rests on linear translation bearings which slides over a rail mounted to a rigid outer steel frame. This mounting method permits us to

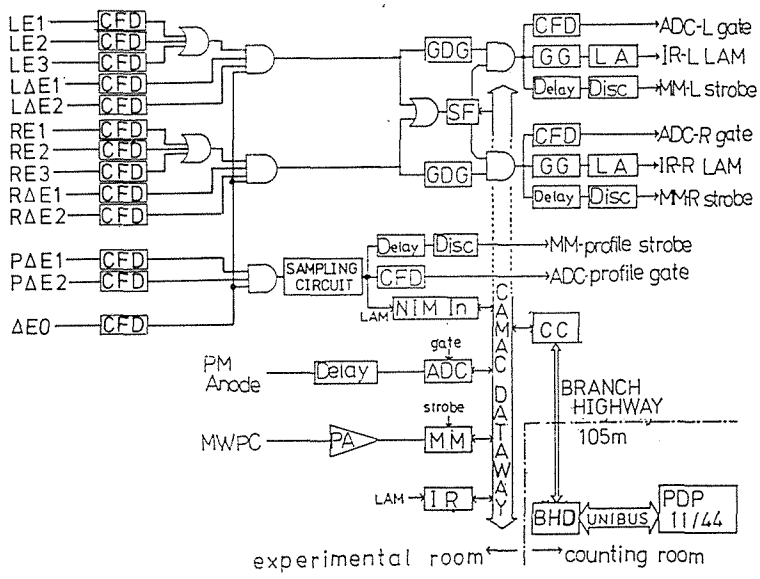

Fig. 7. Block diagram of the electronics.

change the detector geometry easily. To reduce the background, 3 cm thick lead plates and 5 cm thick boron-loaded paraffin plates are attached to the outer rigid frame behind the E-counters.

4.3 Data acquisition

The electronic scheme is outlined in fig. 7. A left event is defined by the logic of $\Delta E0 \cdot L\Delta E1 \cdot L\Delta E2 \cdot (LE1+LE2+LE3)$ (where "$\cdot$" is equivalent to logical 'AND' and "+" is equivalent to logical 'OR') and right event by $\Delta E0 \cdot R\Delta E1 \cdot R\Delta E2 \cdot (RE1+RE2+RE3)$. A profile event is defined by $\Delta E0 \cdot P\Delta E1 \cdot P\Delta E2$. Since the rate of profile events is much higher than those of left and right events, profile events are thinned out by a prescaler. MWPC position signals from about 1000 wires are taken by a CAMAC system. This position data and pulse height data from plastic scintillators are collected by crate controllers located in the experimental area. One event consists of about 44 words. These data are transmitted through a 105 m CAMAC branch highway to the counting room. In the counting room, these data were recorded on the magnetic tape in a list mode by a PDP11/44 computer which monitored position signals from MWPCs and pulse height signals from the plastic scintillators during the experiment. Total dead time for one event including CAMAC operations is about 1400 μs. 70 events per seconds were recorded with 10% loss in typical experimental conditions. Position signals from MWPCs and pulse height signals from the plastic scintillators were monitored continuously during the experiment. This data acquisition system were improved in the course of the experiment and the feature of the development is listed in table 5.

Table 5. Improvement of the online data acquisition system.

MWPC READOUT	CAMAC HIGHWAY	DATA (word)	TIME (μ sec)
not encode	serial	31	2600
not encode	branch	44	1400
encode	branch	22	600

5. Experimental Procedure

5.1 Formalism (refs. 29–30)

In this section we develop the formalism to correct the polaization-transfer observables for out-of- plane scattering effects that tend to mix final-state polarizations. The approach taken here allows for corrections to be made after the "first order" values have been determined. In most cases, corrections to one polarization-transfer observables involve values of other polarization-transfer observables.

In a polarization transfer experiment, it is convenient to express the polarization of projectile in its helicity frame. We consider the polarization transfer measurement for a spin 1/2 projectile and outgoing particle. We define five coordinate systems to

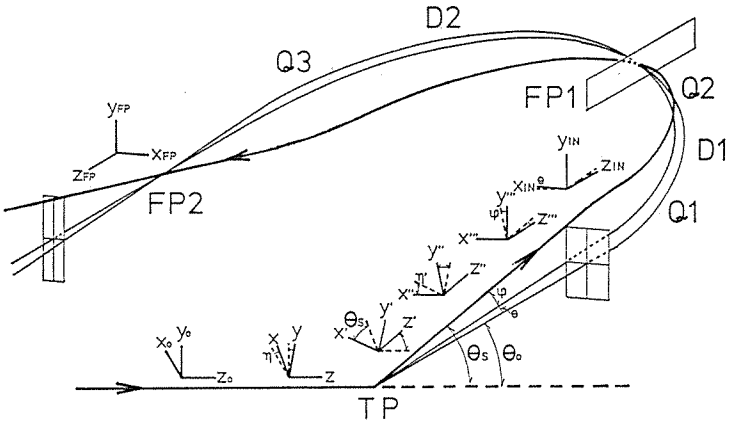

Fig. 8. Definition of the coordinate.

completely describe the scattering process. The first is the "beam-line" system labeled as (x_0, y_0, z_0) in fig. 8. This is used for definition of beam polarization. Second is the "incident-particle" frame given by (x, y, z) (z along k_{in}, y along $k_{in}\times k_{out}$). The "beam-line" and "incident-particle" frames coincide when the azimuthal angle at the target η in fig. 8 is zero. The vertical angle at the target is ϕ, $(\theta+\theta_0)$ is the horizontal, and the true scattering angle at the target is θ_s. The relation between the various angles in fig. 8 is given by:

$$\tan\theta_s = \tan(\theta+\theta_0)\sqrt{1+\tan^2\phi/\sin^2(\theta+\theta_0)}\,, \tag{1}$$

$$\tan\eta = \tan\phi/\sin(\theta+\theta_0)\,,$$

$$\tan\eta' = \sin\phi/\tan(\theta+\theta_0)\,. \tag{2}$$

The third system is the "scattered-particle" frame given by (x', y', z') with $y'=y$, z' along k_{out} (lab) and $x'=y'\times z'$. These frames are shown in fig. 8. The y and y' are identical, but are usually distinguished for the sake of notational consistency. This is an important frame because the actual scattering process is defined in terms of it. Further rotations around z' axis, around x'' axis and around y''' axis are considered. This sixth system is the DUMAS "IN" frame given by (x_{IN}, y_{IN}, z_{IN}). Finally, the actual measurements are made in the FP2 "focal-point" system defined in fig. 8 as (x_{FP}, y_{FP}, z_{FP}). Polarization are calculated for the two transverse components at the focal point p_y (FP) and p_x (FP).

The polarization of the incoming beam measured in the "beam-line" system (x_0, y_0, z_0) is given by:

$$\vec{p}^{\,0}{}_B = \begin{pmatrix} p^0{}_x \\ p^0{}_y \\ p^0{}_z \end{pmatrix}. \tag{3}$$

The same beam polarization measured in the "incident-particle" system (x, y, z) is

given by:

$$\vec{p}_B = \begin{pmatrix} p_x \\ p_y \\ p_z \end{pmatrix} = \begin{pmatrix} \cos\eta & \sin\eta & 0 \\ -\sin\eta & \cos\eta & 0 \\ 0 & 0 & 1 \end{pmatrix} \vec{p}^{\,0}{}_B \,. \tag{4}$$

The polarization of the scattered particle in the "scattered-particle" system (x', y', z') is given by:

$$\vec{p}' = \begin{pmatrix} p'_{x'} \\ p'_{y'} \\ p'_{z'} \end{pmatrix} = \left[\begin{pmatrix} K_x{}^{x'} & 0 & K_z{}^{x'} \\ 0 & K_y{}^{y'} & 0 \\ K_x{}^{z'} & 0 & K_z{}^{z'} \end{pmatrix} \vec{p}_B + \begin{pmatrix} 0 \\ P_{y'} \\ 0 \end{pmatrix} \right] / (1 + p_y A_y) \,, \tag{5}$$

where $K_y{}^{y'}$, $K_x{}^{x'}$, $K_z{}^{z'}$, $K_x{}^{z'}$, and $K_z{}^{z'}$ correspond to the commonly-referred-to Wolfenstein parameters D, R, A, R', and A', respectively. P_y is the polarization and A_y is the vector analyzing power for the reaction. The x' vector is now rotated into the horizontal plane to give:

$$\vec{p}'' = \begin{pmatrix} \cos\eta' & -\sin\eta' & 0 \\ \sin\eta' & \cos\eta' & 0 \\ 0 & 0 & 1 \end{pmatrix} \vec{p}' \,, \quad \vec{p}''' = \begin{pmatrix} 1 & 0 & 0 \\ 0 & \cos\phi & -\sin\phi \\ 0 & \sin\phi & \cos\phi \end{pmatrix} \vec{p}'' \,,$$

$$\vec{p}_{IN} = \begin{pmatrix} \cos\theta & 0 & -\sin\theta \\ 0 & 1 & 0 \\ \sin\theta & 0 & \cos\theta \end{pmatrix} \vec{p}''' \,. \tag{6}$$

The polarization at the focal point is then given by:

$$\vec{p}_{FP} = \begin{pmatrix} \cos\chi & 0 & \sin\chi \\ 0 & 1 & 0 \\ -\sin\chi & 0 & \cos\chi \end{pmatrix} \vec{p}_{IN} \,, \tag{7}$$

where χ is the precession angle of the proton polarization with respect to its momentum and is given by:

$$\chi = \gamma\,(g/2 - 1)\,\omega \sim 331.7\,\gamma \,. \tag{8}$$

γ is the Lorentz factor, $g/2$ is the proton magnetic moment (2.793), and ω is the bend angle in DUMAS (185°). A more complicated expression is needed to transform into the "FP" frame if effects of focusing field are explicitly taken into account. Relying on the ion optical character of DUMAS (see items 3e and 3f in sec. 3.1), we now assume that the precession in DUMAS takes place around the y_{IN} axis only.

We consider the measurement of $K_y{}^{y'}$. The polarization after the first scattering to the left my be written as:

$$p_{y'} = [P_{y'} + p_y K_y{}^{y'}] / [1 + p_y A_y] \,. \tag{9}$$

The number of outgoing particles, n', may be written as:

$$n' = nN\,\Delta\Omega\; I_0[1+p_y\,A_y]\,, \tag{10}$$

where $\Delta\Omega$ is the solid angle of acceptance of analyzing device. The yield, denoted by L, in a second scattering to the left will be:

$$L = n'N^{(2)}\;\Omega_L^{(2)}\;I_0^{(2)}\;[1+p_{y'}\,A_y^{(2)}]\,, \tag{11}$$

where quantities pertaining to the second scattering are indicated by a superscript "2". Substituting eqs. (9) and (10) into eq. (11), we have:

$$L = n\,N\,N^{(2)}\,\Delta\Omega\;\Omega_L^{(2)}\;I_0\,I_0^{(2)}\;[1+p_y\,A_y+(P_{y'}+p_y\,K_y^{y'})\,A_y^{(2)}]\,, \tag{12}$$

and correspondingly, for a second scattering to the right

$$R = n\,N\,N^{(2)}\,\Delta\Omega\;\Omega_R^{(2)}\;I_0\,I_0^{(2)}\;[1+p_y\,A_y-(P_{y'}+p_y\,K_y^{y'})\,A_y^{(2)}]\,. \tag{13}$$

5.2 Measurement Procedure

The depolarization parameter $K_y^{y'}$ for the elastic scattering of 65 MeV polarized protons from deuterium has been measured in the present experiment using a high-intensity polarized beam, a newly designed polarization spectrograph DUMAS and a multi-foil polarimeter MUSASHI.

The experimental procedure used is as follows. The 65 MeV polarized proton beam from the RCNP cyclotron was achromatically transported to the target, and the beam polarization was continuously monitored by a polarimeter placed upstream of the target during the measurements (fig. 9). In order to reduce systematic errors, the beam polarization altered between three modes, spin-up, spin-down and 'unpol', at intervals of 0.5 sec. The 'unpol' beam was produced by switching off the r.f. transitions at the polarized ion source. The typical beam polarization values of spin-up, spin-down and 'unpol' modes were 0.82, -0.80 and 0.03, respectively. After passing through the polarimeter target foil, the beam was focused on the target. A typical beam spot size on the target was 2 mm(W) $\times$ 0.5 mm(H). The beam intensity on the target was typically 300 nA. The target was a self-supporting foil of CD_2 (deuterium enriched, 18.7 mg/cm^2). A carbon foil (natural abundance, 40 mg/cm^2) was also used in order to estimate the background effect of the inelastic scattering from carbon in the CD_2 foil. We limited the beam current on the CD_2 target to 200 nA or less in order to reduce the rate of the decomposition of the target.

The scattered protons were momentum-analyzed and focused dispersively on the first focal plane (FP1) of DUMAS. The solid angle and angular acceptance used were 2.1 msr and $\pm 1.1°$, respectively. In cases where the counting rate of protons elastically scattered by deuterium was very high ($\sim$100 kcps), we used a slit system in front of the tagging counter in order to select only protons elastically scattered by deuterium. A typical momentum spectrum at FP1 is shown in fig. 10. The energy resolution for protons inelastically scattered by carbon was $\pm$90 keV (rms) and was limited by the wire spacing (2 mm) of the chamber.

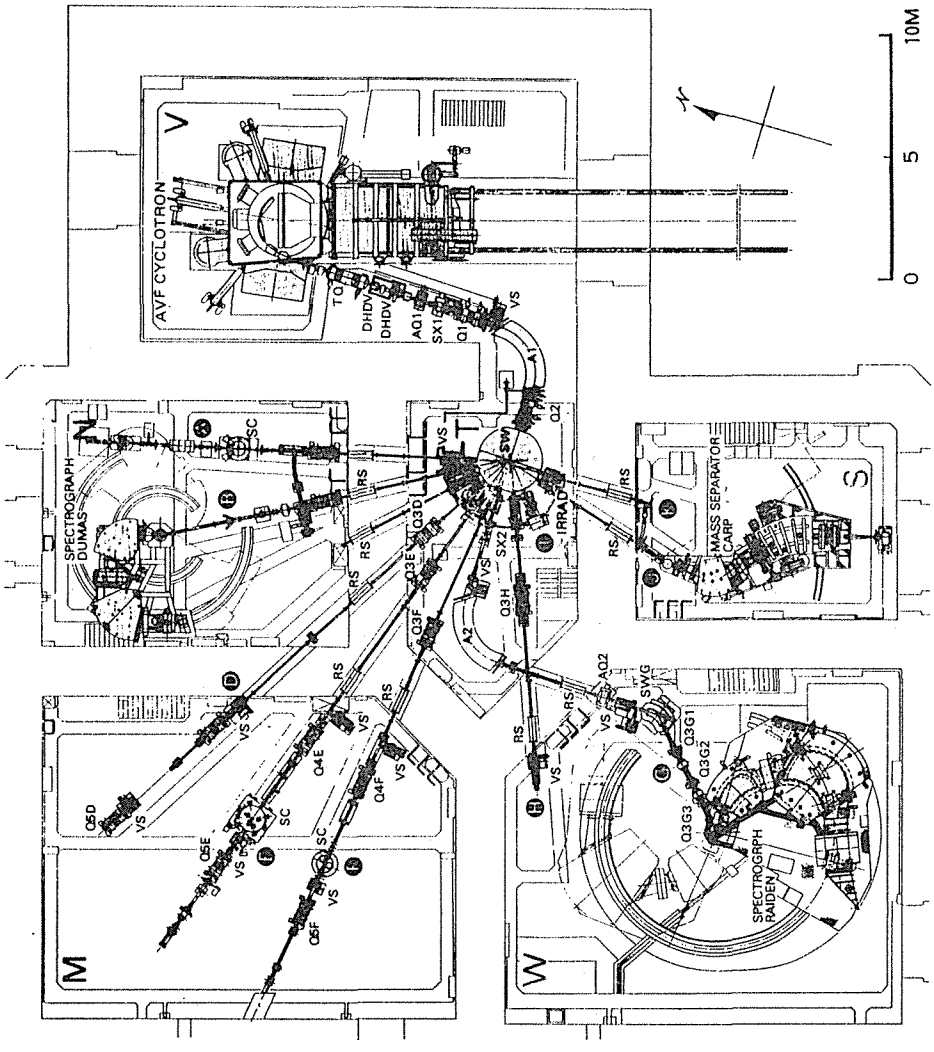

Fig. 9. Layout of the beam transport system at RCNP.

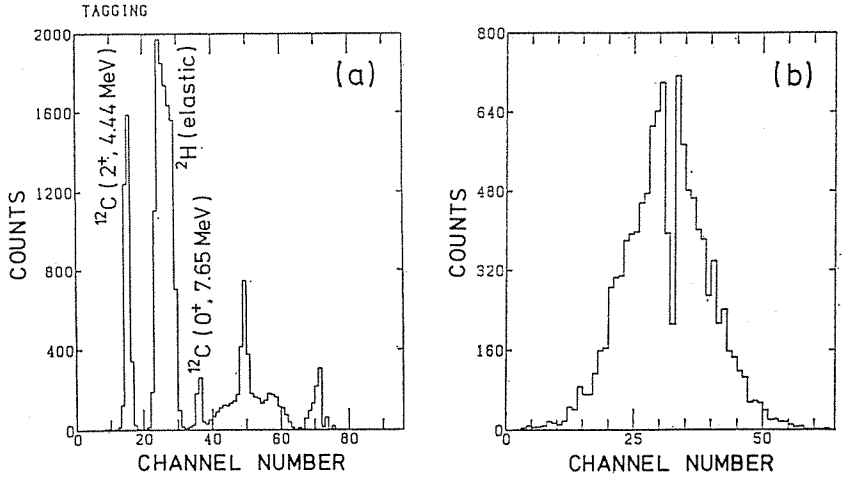

Fig. 10. Position spectrum: a) tagging counter (FP1), b) profile counter (FP2).

Protons which passed through the carbon foils were monitored continuously with two MWPCs (XS, YS) to check the focus at the FP2 (see fig. 10) and were counted as profile events by a pair of plastic scintillators to measure the analyzing power of the first target. The typical spot size was 10 mm(W) × 5 mm(H). At the beginning of every run, we have tuned the position of the focused image by changing the magnetic field of D2 magnet. Typically only 1/10,000 of the profile events was accepted by the read-out system in order to reduce the rate of data acquisition.

6. Data Analysis

6.1 Off-line analysis—Event

There are three types of events, left, right and profile. Left and right events are double scattering events and contain appreciable amounts of chance coincident events at backward angles. In the off line analyses the chance coincident events are rejected by testing the hit of two MWPCs (near and far). But these chance coincident events gave a rather high event rate and consequently a high transmission loss in the on-line data acquisition. Therefore a fourfold coincidence is better to reduce the chance coincidence.

At the first step of the off line analysis, we sorted out good events from bad events, by using the MWPC data.

Good events are:

1) Three MWPCs (tagging, near and far) are fired. If we used the tagging slit, tagging data are not necessary.

2) The number of cluster is one. Populations of the number of clusters and the number of hit wires in a cluster are shown in fig. 11. In the tagging counter the particle track is perpendicular to the counter and scarcely hits the adjacent three wires. The counting rate is very high and the chance coincident two particle hit

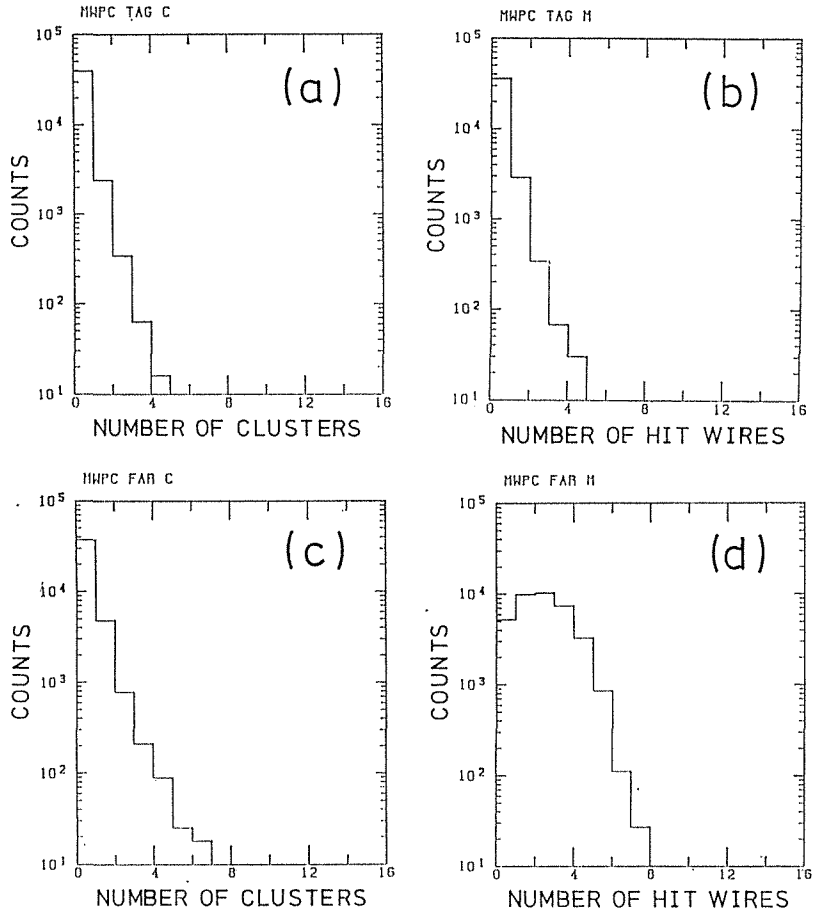

Fig. 11. Distribution of clusters of hit wires in a event: a, c) number of clusters in a event, b, d) number of hit wires in a cluster, a, b) tagging counter, c, d) LL large left MWPC.

two wires. The tagging event with the number of hit wires in a cluster less than three are accepted. On the other hand in left and right MWPCs cover the scattering angles of 30° and 75° and the particle hits two or three wires. Most probable number of his wires is two. In the multi-cluster case one cluster is large but other cluster is small. The ratio of two cluster or more event to the total is less than 5%. The rate of the good events to total is almost the same for spin mode and event type.

6.2 Off-Line analysis—Ray trace

The procedure to construct a final Q-value spectrum from the data on MT is as follows. In the left or ight telescope (LM–LL or RM–RL) of MWPCs, we can trace the proton trajectory back to the central axis of the polarimeter and determine the position of the carbon target and the angle of the scattered proton. The result of the target identification is shown in fig. 12. Each carbon foil is well separated. The

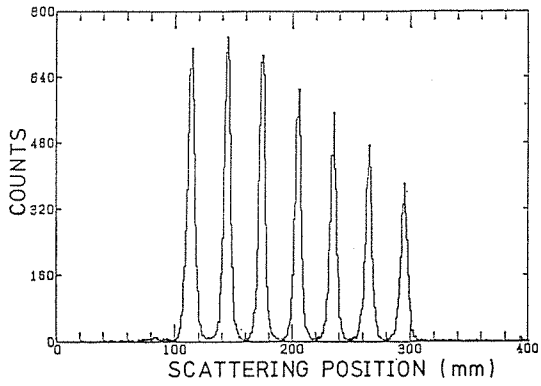

Fig. 12. Distribution of the scattering positions along the central axis of the polarimeter.

polarimeter MUSASHI accepts the events in the angular region between 30° and 80° which covers the optimum regions of the analyzing power in the energy range between 20 MeV and 84 MeV.

6.3 Off-Line analysis—Energy spectrum

A typical energy spectrum for one of the E-counters is shown in fig. 13 for protons scattered from one of carbon foil in the angular range from 45° to 60°. This spectrum is corrected for kinematics in the p–C reaction, energy losses in all materials through which protons have passed, and the position dependence in the E-counters. A typical position dependence is shown in fig. 14. After these corrections the elastic and inelastic (4.44 MeV) peaks from the carbon foil were well separated, but the tails of the peaks overlapped each other slightly. Therefore peak areas were extracted using a peak fitting code for each beam polarization mode. A method for the automatic identification of peaks in a spectrum with a least-square peak fitting routine was used. The peak shape used for these spectra consists of a Gaussian in the top, an

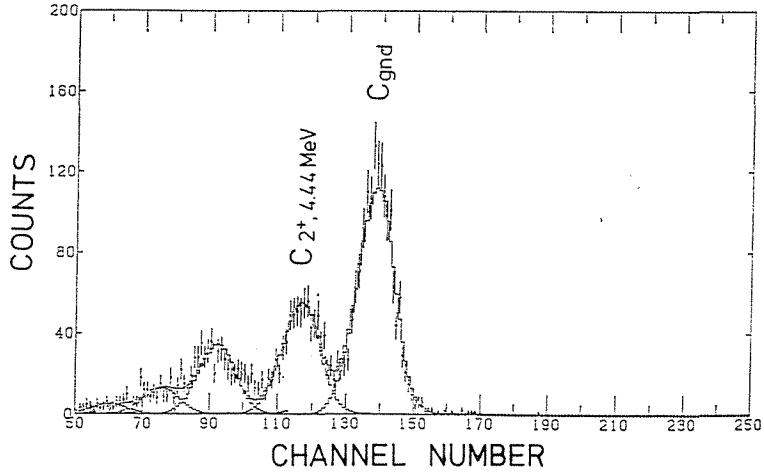

Fig. 13. Energy spectrum of protons scattered from a carbon foil.

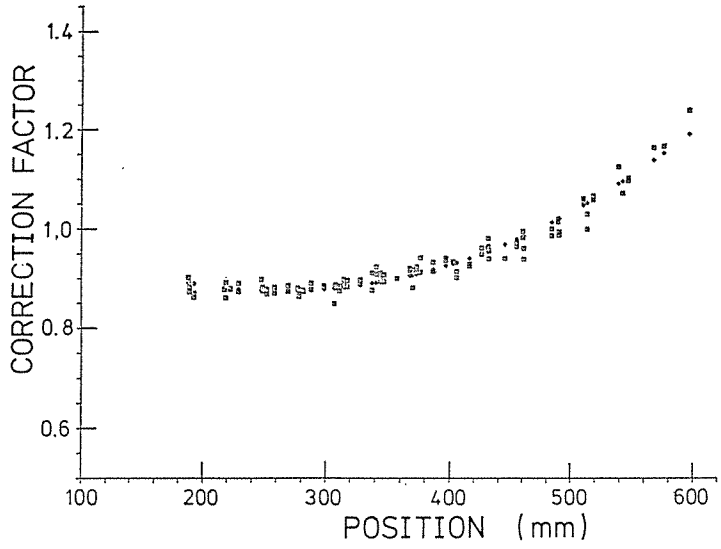

Fig. 14. Position dependence of the correction factor to the pulse height of the scintillator for a shortage of the light collection.

exponential on the right-hand side and a double exponential on the left-hand side (ref. 32).

6.4 $\sigma(\theta)$ and $A_y(\theta)$ in p–C elastic scattering between 20 MeV and 84 MeV (ref. 26)

The p–C elastic scattering data for a wide range of energies and angles are necessary to evaluate the effective analyzing power of the polarimeter MUSASHI. In the energy range of protons between 20 MeV and 84 MeV, p–C elastic scattering has been measured at several laboratories. Although they permitted to forecast the usefulness of the carbon polarimeter in this energy range, the absolute values of cross sections are slightly different each other and some existing measurements were not of sufficient accuracy and angular resolution and steps. There was thus a need for precise measurements of analyzing powers and cross sections for p–C elastic scattering. We have newly measured angular distributions of the cross section $\sigma(\theta)$ and the analyzing power $A_y(\theta)$ in p–C elastic scattering for the angular range between 15° and 80° with 2.5° steps at 19 energies of 21.1, 22.3, 23.5, 24.6, 26.4, 28.1, 29.7, 32.7, 34.5, 39.6, 44.7, 49.6, 54.4, 59.5, 64.9, 69.5, 74.8, 79.8, and 83.4 MeV at the center of the carbon target.

6.5 Effective analyzing power and effective efficiency of the polarimeter MUSASHI

The effective analyzing power and the effective efficiency of the polarimeter MUSASHI can be estimated using the cross section $\sigma(\theta_1, E_p)$ and the analyzing power $A_y(\theta_1, E_p)$ in p–C elastic scattering. The values of $\sigma(E, \theta) \sin\theta$ and $\sigma(E, \theta) A_y$

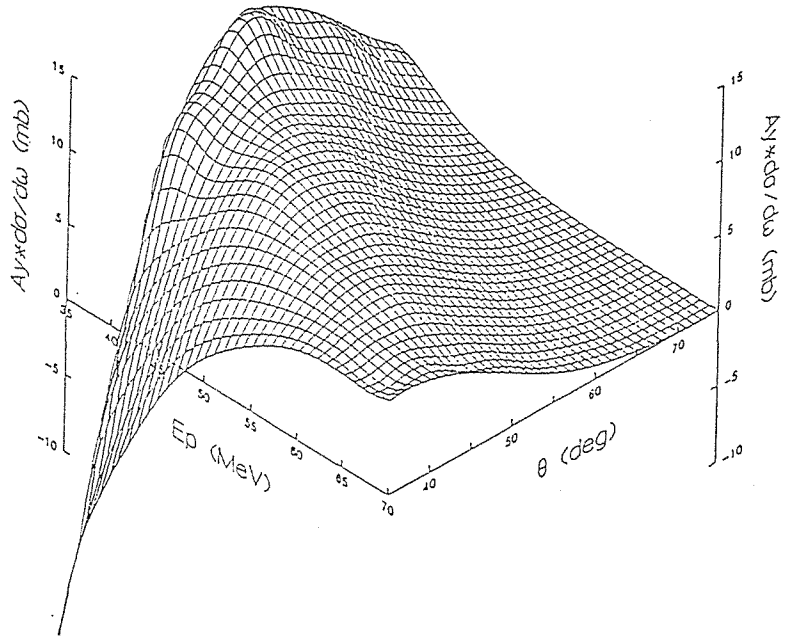

Fig. 15. An example of the interpolation of $A_y \cdot d\sigma/d\Omega$ by the two-dimensional B-spline functions.

(E, θ) $\sin\theta$ from the experimental data were fitted by spline functions (see fig. 15) and were integrated over energy E and scattering angles θ and ϕ. The most efficient way to reduce the statistical error is to choose the maximum figure of merit. It is better to choose so as to reduce the systematic error *e.g.* in the case of improper geometrical adjustment. Another important point is to keep the energy spectrum good and allow the good peak separation in fitting procedure. We fixed the angular width of 10° and used the region where the effective analyzing power is maximum. This region depends on the proton energy entered into the polarimeter MUSASHI and the number of the scattering foils. In the integration over θ, we took into account the effect of the angular spread of the secondary beam and the angular spread due to the multiple scattering in the carbon foils (about $\pm 1.5°$ after passing through all the carbon foils). The effective analyzing power of 0.91 and the effective efficiency of about 1×10^{-4} were used at 64 MeV.

6.6 Ratio

Primary proton beam of polarization p_s was elastically scattered by deuterium, and then the scattered protons were elastically scattered again by carbon foils. By using eqs. (12) and (13) the observed yield of protons N_{slr} is given by:

$$N_{slr} = N_s N_{lr}^{(2)} [1 + p_s A_y + (P_{y'} + p_s K_y^{y'}) A_{ylr}^{(2)}] , \qquad (14)$$

where A_y, $P_{y'}$ and $K_y^{y'}$ are the analyzing power, polarization and depolarization parameter for deuterium, respectively, and N_s is the product of the number of protons

incident on the deuterium target, and target density, the unpolarized cross section and the solid angle for the scattering from deuterium. The quantity $A_{ylr}^{(2)}$ is an effective analyzing power for the scattering from carbon and $N_{lr}^{(2)}$ is the product of the carbon target density, the unpolarized cross section, the solid angle and the counting efficiency for the scattering from carbon.

In order to reduce systematic errors, the following ratio (left/right ratio) is determined by:

$$\frac{N_{\uparrow l}\,N_{\downarrow r}}{N_{\downarrow l}\,N_{\uparrow r}}=\frac{1+p_{\uparrow}\,A_y+(P_{y'}+p_{\uparrow}\,K_y{}^{y'})\,A_{yl}{}^{(2)}}{1+p_{\downarrow}\,A_y+(P_{y'}+p_{\downarrow}\,K_y{}^{y'})\,A_{yl}{}^{(2)}}\,\frac{1+p_{\downarrow}\,A_y+(P_{y'}+p_{\downarrow}\,K_y{}^{y'})\,A_{yr}{}^{(2)}}{1+p_{\uparrow}\,A_y+(P_{y'}+p_{\uparrow}\,K_y{}^{y'})\,A_{yr}{}^{(2)}}\,. \tag{15}$$

The depolarization parameter $K_y{}^{y'}$ is then extracted from above ratio (which is independent of the detector solid angles and efficiencies) in terms of the five measured (or calculated) values of N_{slr}, p_s, A_y, $P_{y'}$ and $A_{ylr}{}^{(2)}$.

N_{slr}: These values were obtained by peak fitting procedure.

p_s: Beam polarizations are obtained for three modes.

A_y: The analyzing power was obtained by using profile events. These measurements of the analyzing power were consistent with the measurements by Shimizu et al. (ref. 30).

$P_{y'}$: The polarization $P_{y'}$ obtained by direct measurements in this experiment using an unpolarized beam agreeds with the analyzing power A_y within the experimental errors. Since a measurable breaking of the time reversal invariance is unlikely in the elastic scattering, we assumed $P_{y'}=A_y$. The effect of the depolarization due to the spin precession by the magnetic field in passing through the DUMAS system was estimated to be less than 0.003.

$A_{ylr}{}^{(2)}$: The effective analyzing power were obtained as described before.

7. Experimental Result

In order to check the measurement system, $K_y{}^{y'}$ for the elastic and inelastic (0^+, 7.65 MeV) scattering from carbon (natural) was measured, because this must be equal to unity under the parity conservation for a spin 0 nucleus. The effect of the depolarization of ^{13}C (isotopic abundance 1.1%) included in the natural carbon was estimated to be less than 0.001 because the depolarization of ^{13}C is about 0.95 at most (ref. 13). The $K_y{}^{y'}$ data for the elastic scattering from carbon (natural) were equal to unity within measurement errors (typically 1.0065 ± 0.0080 at 35.5°). Fig. 16 shows system checks using the $K_y{}^{y'}$ for the elastic scattering from ^{24}Mg.

Because a CD_2 foil was used as the primary target, the elastic scattering peak from deuterium overlapped with an inelastic scattering peak from carbon at the laboratory angles of 23°, 31°, and 35°. In these cases the depolarization parameter for the inelastic scattering was measured separately with a carbon foil target, and this information was used to subtract the contribution of carbon inelastic scattering to the total yield.

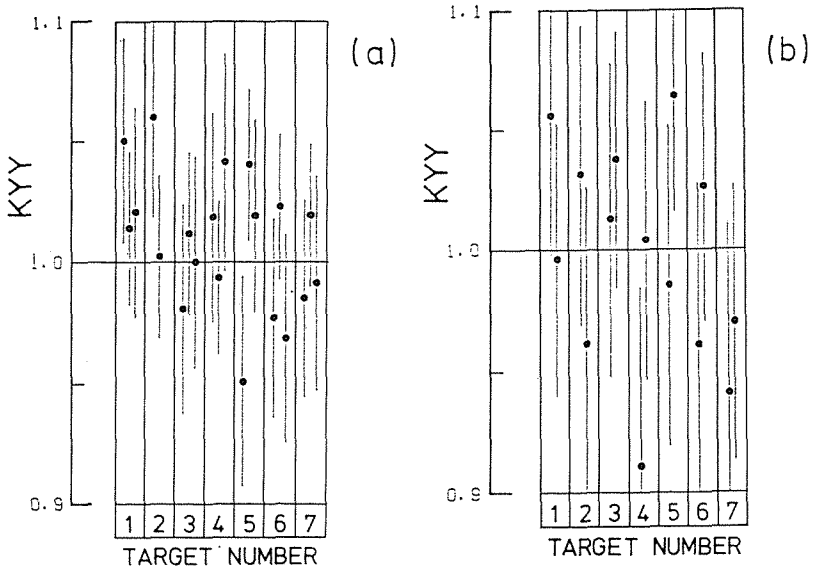

Fig. 16. Results of the system check: a) left/right ratio, b) elastic/inelastic ratio.

$$\overline{K_y^{y'}} = (K_y^{y'} + \alpha\, K_y^{y'inl})/(1+\alpha)$$
$$\overline{A_y} = (A_y + \alpha\, A_y^{inl})/(1+\alpha)$$
$$\overline{P_{y'}} = (P_{y'} + \alpha\, P_{y'}^{inl})/(1+\alpha)\ ,$$

where α is the ratio of the carbon inelastic peak to the deuteron elastic peak. $\overline{K_y^{y'}}$, $K_y^{y'}$ and $K_y^{y'inl}$ are the depolarization parameters for the overlapped peak, the deuteron peak, and inelastic peak, respectively, and so on.

7.2 Results

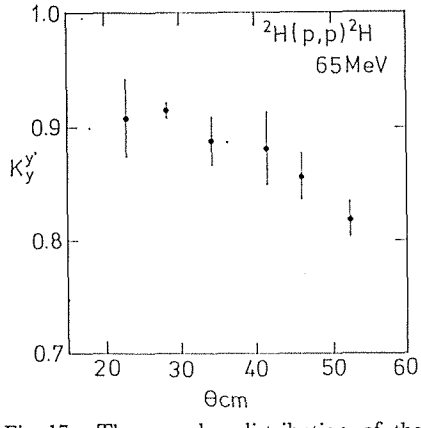

Fig. 17. The angular distribution of the depolarization parameter $K_y^{y'}$ for p-²H elastic scattering at E_p=65 MeV.

Table 6. The depolarization parameter $K_y^{y'}$ in p–²H elastic scattering at E_p=65 MeV

ANGLE cm (deg)	$K_y^{y'}$	$dK_y^{y'}$
22.8	0.9085	0.0342
28.8	0.9149	0.0064
34.8	0.8879	0.0211
41.4	0.8563	0.0199
46.6	0.8563	0.0199
52.4	0.8185	0.0159

The angular distribution of the measured depolarization parameter $K_y{}^{y'}$ for elastic scattering from deuterium is shown in fig. 17 (ref. 33). The error bars are mainly due to counting statistics but also include the errors in the peak fitting of the energy spectrum of the plastic scintillators and the errors in the subtraction of the carbon inelastic peak in the overlapping cases. As can be seen from this figure, the observed $K_y{}^{y'}$ data deviate significantly from unity and decrease as the scattering angle increases.

8. Comparison with Faddeev Calculation

8.1 Faddeev formalism

The Faddeev results were calculated with the computer code by Koike and Taniguchi (ref. 34). The AGS formalism (ref. 35) is used to analyze the neutron-deuteron scattering. Essentials of the formalism are described in textbooks for the general three-body system (refs. 36–37). We give the outline of the formalism in order to clarify the definitions and the notations.

The three-body equations are the coupled equations for the operator $U_{sa'}(E)$ which operates on the three-body Hilbert space:

$$U_{aa'}(E) = (E-H_0)\,(1-\delta_{aa'}) + \sum_{a''\neq a} T_{a''}(E)\, G_0(E)\, U_{a''a'}(E)\,, \qquad (17)$$

$$\text{with} \quad a, a', a'' = 1, 2, 3\,,$$

where the dynamical input is the two-body t-operator $T_a(E)$; E is the three-body energy. The indices a, a', a'' represent particle channels or partitions.

A two-body partial wave expansion of T_a is introduced by:

$$T_a = \sum_{\sigma} P^{\sigma}{}_a\, T^{\sigma}{}_a\,, \qquad (18)$$

where P^{σ} is a projection operator onto the partial wave of interacting pairs, which is characterized by the total angular momentum (j), isospin (i), and the parity (π).

It is assumed that each partial wave t-matrix T^a is well approximated by a separable form with rank N:

$$T^{\sigma}{}_a(\varepsilon) = \sum_{n,m=1}^{N} g^{\sigma}{}_{an}\, \tau^{\sigma}{}_{anm}(\varepsilon)\, g^{\sigma}{}_{am}\,. \qquad (19)$$

A rank-N separable potential is assumed in each state in order to produce a rank-N separable t-matrix retaining unitarity and analyticity. We drop the suffix a, since all partition are equivalent. The potential in σ is written as:

$$V = \sum_{n,m=1}^{N} g^{\sigma}{}_n\, \lambda^{\sigma}{}_{nm}\, g^{\sigma}{}_m\,. \qquad (20)$$

8.2 Separable potential

Up to now, accurate three-body calculations especially for scattering with polarization have been done with using separable t-matrices. Two different approaches have been used to solve the three -nucleon scattering problem. One of them is to

Table 7. Separable potential sets used in the Faddeev calculations.

Potential set	Partial waves			
	$^1S_0$	$^3S_1$–$^3D_1$	$^1P_1$	$^1D_2$
			$^3P_{0,1,2}$	$^3D_{2,3}$
PEST3–PEST4–P–D	PEST3	PEST4	P	D
BEST3–BEST4–P–D	BEST3	BEST4	P	D
GRAZII–GRAZII–P–D	GRAZII	GRAZII	P	D
1Y–4T4B–P–D	1Y	4T4B	P	D

use separable t-matrices derived from phenomenological separable potentials. The other is to use a separable representation of any potentials by means of the Ernst-Shakin-Thaler (EST) method. Both types of separable potentials are used here. The potential sets used are tabulated in table 7. For the $^1S_0$ and $^3S_1$–$^3D_1$ angular momentum states four potential sets were used.

PEST3–PEST4 (refs. 38–39)

A separable representation of the Paris potential is constructed by means of the EST method. These potentials have been constructed to give an accurate representation of both the on-shell and off-shell behaviors of the Paris potential, and reproduce the experimental phase shifts with a good accuracy up to about 400 MeV. The $^3S_1$–$^3D_1$ mixing parameter is reproduced reasonably well up to 200 MeV.

BEST3–BEST4 (ref. 40)

A separable representation of a boson-exchange nucleon-nucleon potential is constructed via the EST method. The resulting separable potential is provided for a satisfactory approximation of the on-shell as well as off-shell properties of the Bonn potential.

GRAZII–GRAZII (ref. 41)

A separable potential is proposed for the n–p interaction in $^1S_0$ and $^3S_1$–$^3D_1$ partial waves. In the singlet S state the potential fits new phenomenological phases rather accurately in the laboratory kinetic energy range of 0–600 MeV; it is also capable of reproducing singlet effective-range parameters in close agreement with the experimental results. In the coupled state $^3S_1$–$^3D_1$ the potential provides a correct description of the deuteron data (E_D, p_D, Q, η), while at the same time it adequately fits modern phenomenological phases up to $E_{lab} \geqq 500$ MeV in both the S and D waves. Only mixing parameter ε_1 deviates from predictions of phase shift analyses. In the construction of the potential a care was taken that its off-shell behavior be reasonable. As an eminent property it thus exhibits an off-shell behavior similar to the one of the Paris potential.

1Y–4T4B (ref. 42–43)

A rank-1 separable potential with a Yamaguchi-type form factor (1Y) is used

for the $^1S_0$ wave (ref. 42). A four-term (M=4) $^3S_1$–$^3D_1$ tensor interaction, which is denoted by 4T4B, was used (ref. 43). This interaction, which yields a 4% D-state probability for deuteron, fits well the $^3S_1$ and $^3D_1$ phases up to 300–400 MeV, and also yields a reasonable fit to the mixing parameter ϵ_1.

P–D (ref. 43)

For other partial waves, Doleschall's rank-1 potentials (P for $^1P_1$ and $^3P_{0,1,2}$ waves and D for $^1D_2$ and $^3D_{2,3}$ waves) are used. The P- and D-state interactions fit the phase shifts. The fits are quite good up to an NN laboratory energy of about 50–100 MeV for the $^3P_0$ interactions and about 300–400 MeV for the D and other P interactions.

8.3 Numerical calculation

Because of the well-known difficulty of treating the Coulomb force exactly in the three-body calculation, the Coulomb effect was treated in an approximated way. The scattering amplitude for p–d scattering was obtained by simply combining the amplitudes obtained from the n–d Faddeev calculations with phases and amplitudes for point like Coulomb scattering, as suggested by Doleschall *et al.* (ref. 44)

$$T^{(p-d)}{}_{LL'} = T^{(p-d)}{}_{LL'} \exp\left[i(\sigma_L+\sigma_{L'})\right] + T^{(Coul)}{}_{LL'} .$$

where σ_L and $\sigma_{L'}$ are Coulomb phases and the L and L' are the angular momentum of p–d two-body system in the final and initial states, respectively.

8.4 L dependence

In this paper, we use the two-nucleon interaction with partial waves up to D waves ($^1S_0$, $^3S_1$–$^3D_1$, $^1P_1$, $^3P_{0,1,2}$, $^1D_2$ and $^3D_{2,3}$ partial waves). If the number of partial waves used in the three-body calculation is small, the calculated result is not accurate. It is important to examine the effect of P and D waves in the calculated results.

In this subsection, we compare the calculated results with PEST3–PEST4, PEST3–PEST4–P and PEST3–PEST4–P–D. We show the integrated total cross

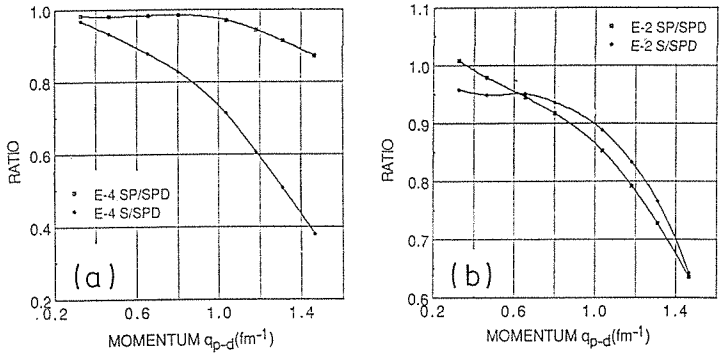

Fig. 18. Effect of P and D waves of the two-nucleon interaction on the total cross section of the nuetron-deuteron scattering. The effects are shown as ratios: a) quartet state, b) doublet state.

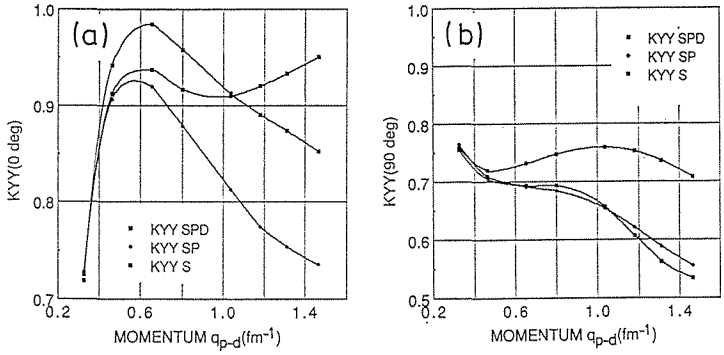

Fig. 19. Effect of P and D waves of the two-nucleon interaction on the depolarization parameter of the nuetron-deuteron scattering: a) $K_y^{y'}$ (0°), b) $K_y^{y'}$ (90°).

section (quartet states E-4 and doublet state E-2). The values from PEST3–PEST4 (S) and PEST3–PEST4–P (S–P) divided by the value from PEST3–PEST4–P–D (S–P–D) are shown in fig. 18. The S–P–D calculation is seem to be sufficient for the E-4 at 65 MeV. For the E-2, P waves become important above $q_{p-d}=0.5$ fm^{-1} and D waves become important above $q_{p-d}=1.0$ fm^{-1}. It correspond to $q_{p-d}=1.5$ fm^{-1} for F waves and at 65 MeV F waves do not become important. In fig. 19 we show the depolarization parameter for elastic n–d scattering at 0° and 90°. It is seen that D waves become important above 50 MeV.

8.5 Comparison

The curves in fig. 20 represent the calculations based on the Faddeev equations and using several separable potential sets which include the $^1S_0$, $^3S_1$–$^3D_1$, $^1P_1$, $^3P_{0,1,2}$, $^1D_2$ and $^3D_{2,3}$ partial-wave interactions. The potential sets used are PEST3–PEST4–

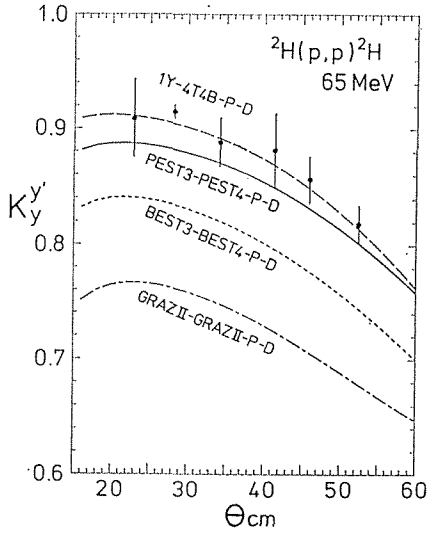

Fig. 20. The angular distribution of the depolarization parameter $K_y^{y'}$ for p-²H elastic scattering at E_p=65 MeV.

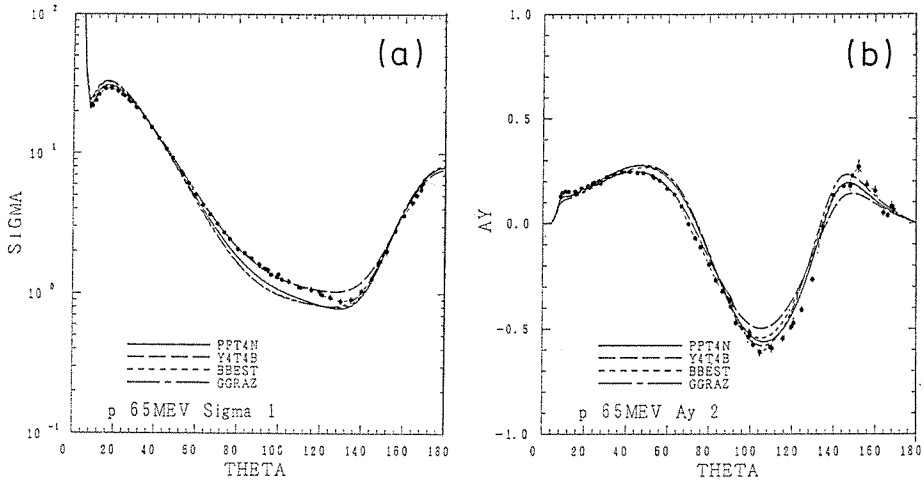

Fig. 21. The angular distribution of the cross section and analyzing power for p-^{2}H elastic scattering at E_p=65 MeV.

P–D, BEST3–BEST4–P–D, GRAZII–GRAZII–P–D and 1Y–4T4B–P–D.

The calculation with 1Y–4T4B–P–D potential set reproduced the measured $K_y^{y'}$ very well. The potential set PEST3–PEST4–P–D reproduces the data fairly well but the other two potential sets do not reproduce the data. Comparison with the measured cross section and analyzing power and calculations are shown in fig. 21. All of these potential sets reproduce the measured cross sections and the analyzing powers well. The 1Y–4T4B–P–D potential set also reproduces the data best at forward angles of less than 90°. It should be noted that the differences among the calculations with four potential sets are very small at backward angles larger than 140°.

We examine the effects due to the potential difference in $^1S_0$ and $^3S_1$–$^3D_1$ waves (see fig. 22). All of the potentials used reproduce both $^3S_1$ and $^3D_1$ phase shifts but they have different behavior in the $^3S_1$–$^3D_1$ mixing parameter ε_1. The 4T4B potential reproduces the empirical mixing parameter, but the GRAZII potential gives a too large value as is shown in fig. 23. The measured $K_y^{y'}$ is thus seen to be reproduced only when a correct on-shell tensor potential (4T4B) is used in the calculation.

On the other hand, the $^3S_1$ ($^1S_0$) PEST, BEST and GRAZII potential seems to have more reasonable off-shell behavior than the 4T4B (1Y) potential since the half-off-shell function in the momentum space of the GRAZII potential has a node like the Paris potential. Experimentally, at E_p=65 MeV the off-shell properties in the $^3S_1$ wave do not seem to have a significant effect on the $K_y^{y'}$. With regard to the $^1S_0$ wave, the calculations with the various $^1S_0$ potentials are almost the same, especially at forward angles.

8.6 Energy dependence

It is interesting to compare separately the contribution of quartet and doublet states to the total cross section. In fig. 24 we see that the doublet amplitudes is very

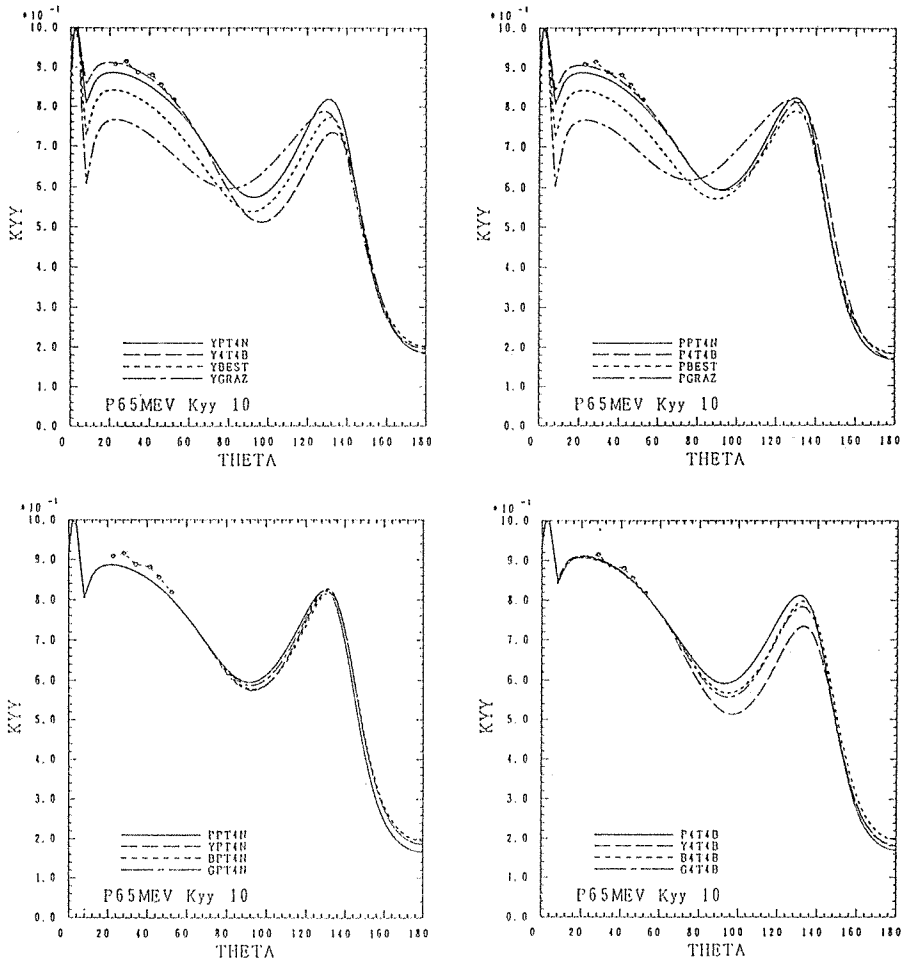

Fig. 22. Calculations of the angular distribution of $K_y{}^{y'}$ with various $^1S_0$ and $^3S_1$–$^3D_1$ potentials.

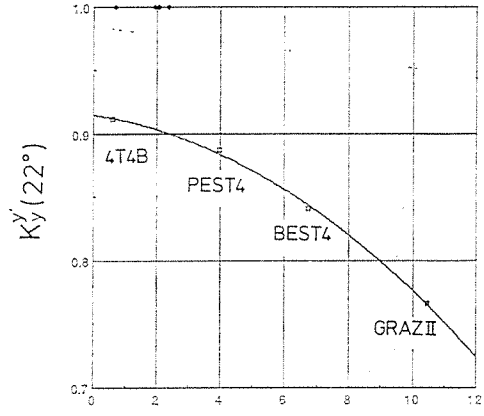

Fig. 23. $^3S_1$–$^3D_1$ miting parameter, ϵ_1, versus $K_y{}^{y'}$ at 22°.

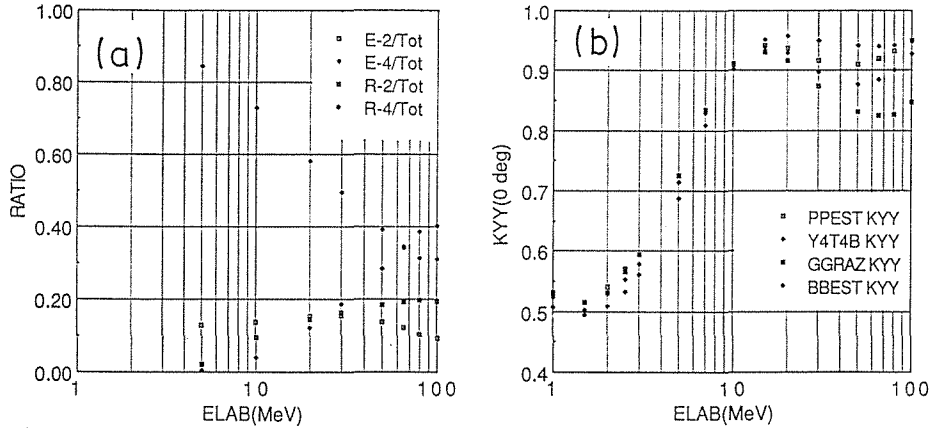

Fig. 24. Energy dependences of a) ratios of integrated cross sections to total cross sections, and b) depolarization parameter $K_y{}^{y'}$ at 0° of the nuetron-deuteron scattering.

small at low energies. Even at 65 MeV, the doublet contribution is very much smaller than quartet beyond the 2 to 1 statistical weight. If at a given angle there are just two-channel spin amplitude: $F_{S',s';s,s}(\theta)=\delta_{S',S}\,\delta_{s',s}\,F_s(\theta)$ which we will denote by F_4 and F_2. It is then straight forward to compare the Wolfenstein parameters (the subscript S stands for S-wave forces) (ref. 4 5):

$$\begin{aligned} D_S &= 2\,(10|F_4|^2+|F_2|^2+16Re\,F_4{}^*F_2)/(9T) \\ T &= Tr\,(F^+F) = 4|F_4|^2+2|F_2|^2 \\ &= 6\,p^2\,\mathrm{d}\sigma/\mathrm{d}\Omega \end{aligned} \tag{22}$$

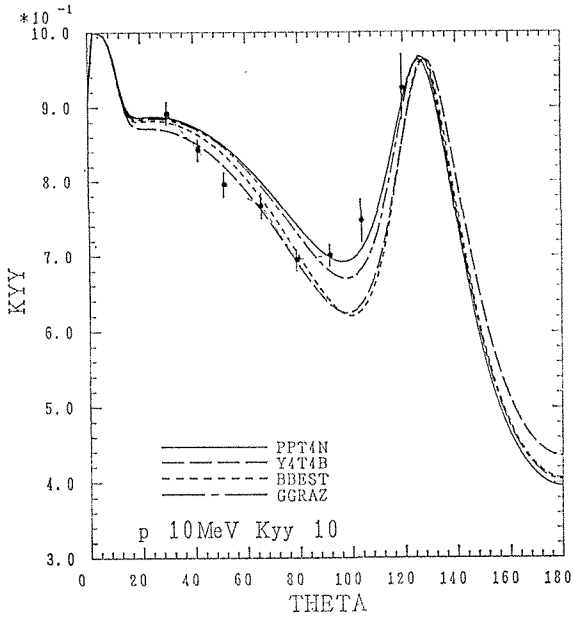

Fig. 25. The angular distribution of the depolarization parameter $K_y{}^{y'}$ for p–^{2}H elastic scattering at E_p=10 MeV.

In AAY (ref. 6) it is shown that the scattering is almost completely in the quartet state at low energies. If we assume in eq. 22 that $F_2=0$ then $D_S=5/9$. The calculated $K_y^{y'}$ values are close to this value at low energies (see fig. 24)

E_p=10 MeV (ref. 46)

There are the data of the depolarization and also 25 observables. Sperisen reported that the depolarization measurement was sensitive to the two-body off-shell interaction. Their depolarization data are shown in fig. 25. The lines are the calculation with the same potential sets as at 65 MeV. The difference in $^1S_0$ wave results very small difference and $^3S_1$–$^3D_1$ waves make some difference. PEST4, BEST4 and GRAZII are like but 4T4B is different from them. Thus the calculation shows some off-shell effect, but all these calculations fail to reproduce the data. The difference among the potential sets are seen more clearly at lower energy (ref. 47).

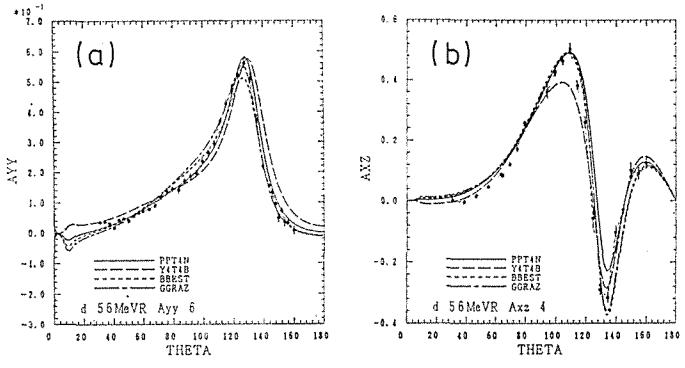

Fig. 26. Angular distributions of the tensor analyzing powers for d–^{1}H elastic scattering at E_d=56 MeV.: a) tensor analyzing power $A_y^{y'}$, b) tensor analyzing power $A_y^{y'}$.

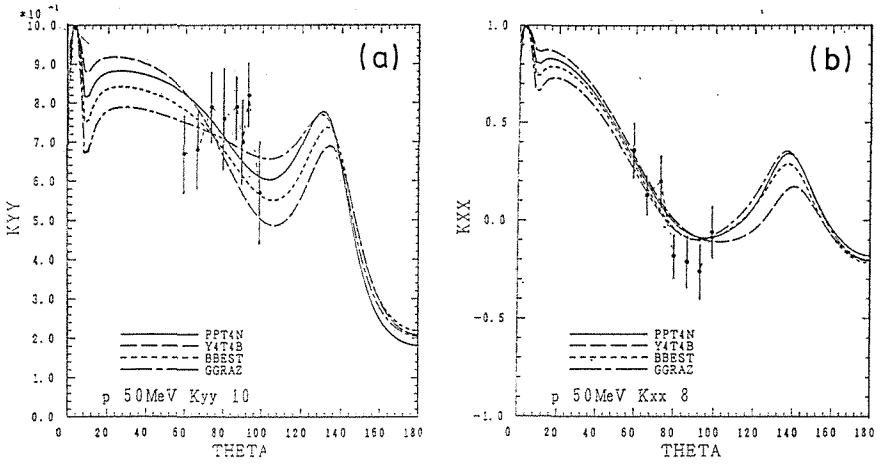

Fig. 27. Angular distributions of the polarization transfer parameters for p–^{2}H elastic scattering at E_p=50 MeV: a) depolarization parameter $K_y^{y'}$, b) polarization transfer parameter $K_x^{x'}$.

E_d=56 MeV (ref. 48)

In this energy there is no depolarization data. But tensor analyzing powers were measured and it is interesting to compare the data with the calculation of the different tensor potentials used here. The data are shown in fig. 26. Here we normalized the original data using the high accuracy carbon data for the beam polarimeter (ref. 49). The tensor analyzing powers at E_d=56 MeV are reproduced by the tensor potentials which give a deuteron D-state probability of 4%–5%, and there is no appreciable difference among the calculated values with the PEST4, BEST4, GRAZII and 4T4B potentials.

E_p=50 MeV (ref. 50)

In this energy the depolarization was measured up to 90° and there are some differences among the calculated values (see fig. 27). But the experimental error was large and it is not difficult to extract the information on the interaction.

9. Conclusion

In summary, a newly designed spectrograph has been constructed in order to measure spin transfer coefficients. The depolarization parameter $K_y{}^{y'}$ for the elastic scattering of 65 MeV polarized protons from deuterium has been measured using the spectrograph and a multi-foil polarimeter. Faddeev calculations using various types of nucleon-nucleon (N–N) interactions in a separable representation are compared with the data. The measured $K_y{}^{y'}$ values are well reproduced by a calculation using the N–N interaction with a tensor force which is adjusted to reproduce the empirical mixing parameter of the $^3S_1$–$^3D_1$ partial waves. A separable representation of the Paris potential by means of the EST method (PEST4) can not reproduce the data well. The off-shell properties of the interaction seem to have no significant effect on $K_y{}^{y'}$ at forward angles. It thus seems important to measure $K_y{}^{y'}$ at backward angles in order to see the off-shell effect, if any.

Acknowledgments

I wish to express my thanks to the members of the DUMAS constructing group and of our collaborators: Profs. S. Kobayashi and H. Sakaguchi, and Mr. M. Yosoi of Kyoto University, Prof. H. Ikegami and Dr. T. Noro of the Research Center for Nuclear Physics (RCNP), Osaka University, Mr. M. Ieiri and Dr. H. Sakamoto of National Laboratory for High Energy Physics, Dr. H. Ogawa of Nara Women's University, Dr. T. Ichihara of Institute of Physical and Chemical Research, and Mr. N. Isshiki of Sanyo Electro Co., Ltd. I wish to express my thanks to Prof. P. Schwandt of Indiana University Cyclotron Facility who was our collaborator and proposed this experiment for the first polarization transfer experiment using DUMAS and Mr. T. Takayama of Sumitomo Heavy Industries Ltd who was the member of the DUMAS constructing group. Special thanks also go to Prof. S. Kobayashi of Kyoto University who proposed the DUMAS project and has encouraged me through the

experiment. My thanks also go to Prof. Koike of Hosei University who discussed with me and allowed me to use their computer code. I wish to express thanks to Prof. Morinobu of the RCNP for his help during the construction and the staff of the cyclotron at the RCNP for their kind cooperation during the experiment. The data reduction was performed with the computers FACOM M-180-2AD and FACOM M-200 at the RCNP and the Faddeev calculations were performed with the computer FACOM M-340 at the Department of Physics, Kyoto University. The experiment was performed at the RCNP, Osaka University, under Program Nos. 16A14 and 18A05.

References

1) R. A. Arndt *et al.*, Phys. Rev. **D28** (1983) 97.
2) D. V. Bugg, J. Phys. G: Nucl. Phys. **6** (1980) 1329.
3) M. Lacombe *et al.*, Phys. Rev. **C21** (1980) 861.
4) R. Machleidt and K. Holinde, in Few-Body Problems in Physics, Vol. II, edited by B. Zeitnitz (North-Holland, Amsterdam, 1984), p. 79.
5) L. D. Faddeev, Sov. Phys. JETP **12** (1961) 1014.
6) R. Aaron, R. D. Amado and Y. Y. Yam, Phys. Rev. **140** (1965) B 1291.
7) D. J. Ernst, C. M. Shakin and R. M. Thaler, Phys. Rev. **C8** (1973) 46.
8) Y. Koike and Y. Taniguchi, Phys. Lett. **118B** (1982) 248.
9) M. J. Moravcsik, H. M. Sinky and G. R. Goldstein, Annals of Physics **171** (1986) 205.
10) R. D. Ransome *et al.*, Nucl. Instr. and Meth. **201** (1982) 309.
11) G. Waters *et al.*, Nucl. Instr. and Meth. **153** (1978) 401.
12) T. A. Carey *et al.*, Phys. Rev. Lett. **49** (1982) 266.
13) M. Nakamura *et al.*, Nucl. Instr. and Meth. **212** (1983) 173.
14) C. Tschalar, C. J. Batty and A. I. Kilvington, Nucl. Instr. and Meth. **78** (1970) 141.
15) J. M. Moss, D. R. Brown and W. D. Cornelius, Nucl. Instr. and Meth. **135** (1976) 139.
16) W. Gruebler *et al.*, Nucl. Instr. and Meth. **190** (1981) 295.
17) W. Kretschmer *et al.*, Nucl. Instr. and Meth. **A241** (1985) 480, and **A245** (1986) 438.
18) H. Ikegami *et al.*, RCNP Annual Report (1981) p. 179.
19) T. Noro *et al.*, J. Phys. Soc. Jpn. **55** (1986) Suppl. p. 470.
20) H. Ikegami, BUTURI **34** (1979) 778.
21) S. Morinobu, private communication.
22) T. Matsuo *et al.*, Mass Spectroscopy, **24** (1976) 19.
23) S. Morinobu, private communication.
24) S. B. Kowalski and H. A. Enge, Nucl. Instr. and Meth. **A258** (1987) 407.
25) A. M. Winslow, UCRL 7784-T, Rep. 2 (1964); J. Comput. Phys. **1** (1966) 149.
26) M. Ieiri *et al.*, Nucl. Instr. and Meth. **A257** (1987) 253.
27) R. Bouclier *et al.*, Nucl. Instr. and Meth. **88** (1970) 149.
28) G. Charpak *et al.*, Nucl. Instr. and Meth. **99** (1972) 279.
29) G. G. Ohlsen, Rep. Prog. Phys. **35** (1972) 717.
30) J. B. McClelland *et al.*, Los Alamos National Laboratory report LA-UR-84-1671.
31) H. Shimizu *et al.*, Nucl. Phys. **A382** (1982) 242.
32) H. P. Blok, J. C. DE Lange and J. W. Schotman, Nucl. Instr. and Meth. **128** (1975) 545.
33) M. Nakamura *et al.*, Phys. Lett. **B188** (1987) 21.
34) Y. Koike and Y. Taniguchi, Few-Body System **1** (1986) 13.
35) E. O. Alt, P. Grassberger and W. Sandhas, Nucl. Phys. **B2** (1967) 167.
36) I. R. Afnan and A. W. Thomas, in Modern Three-Hadron Physics (Topics in Current Physics, Vol. 2) (A. W. Thomas ed.), p. 1. Berlin —Heiderberg— New York: Springer 1977.
37) E. W. Schmid and H. Ziegelmann, The Quantum Mechanical Three-Body Problem. Oxford:

Pergamon Press 1974.
38) J. Haidenbauer and W. Plessas, Phys. Rev. **C32** (1985) 1424.
39) J. Haidenbauer and W. Plessas, Phys. Rev. **C30** (1984) 1822.
40) J. Haidenbauer, Y. Koike and W. Plessas, Phys. Rev. **C33** (1986) 439.
41) L. Mathelitsch, W. Piessas and W. Schweizer, Phys. Rev. **C26** (1982) 65.
42) A. C. Phillips, Nucl. Phys. **A107** (1968) 209.
43) F. D. Correll *et al.*, Phys. Rev. **C23** (1981) 960.
44) P. Doleschall *et al.*, Nucl. Phys. **A380** (1982) 72.
45) S. C. Pieper, Nucl. Phys. **A193** (1972) 529.
46) F. Sperisen *et al.*, Phys. Lett. **102B** (1981) 9.
F. Sperisen *et al.*, Nucl. Phys. **A422** (1984) 81.
47) H. Zankel and W. Plessas, Z. Phys. **A317** (1984) 45.
B. Loiseau *et al.*, Phys. Rev. **C32** (1985) 2165.
48) K. Hatanaka *et al.*, Nucl. Phys. **A426** (1984) 77.
49) S. Kato *et al.*, Nucl. Instr. and Meth. **A238** (1985) 453.
50) N. M. Stewart *et al.*, Nucl. Phys. **A171** (1971) 225.
N. M. Stewart *et al.*, Nucl. Phys. **A174** (1971) 338.